PERGAMON

International Journal of Solids and Structures 38 (2001) 6275–6305

INTERNATIONAL JOURNAL OF SOLIDS and STRUCTURES

www.elsevier.com/locate/ijsolstr

Collapse of truss core sandwich beams in 3-point bending

V.S. Deshpande, N.A. Fleck *

Department of Engineering, University of Cambridge, Trumpington Street, Cambridge CB2 1PZ, UK

Received 11 December 2000; in revised form 30 April 2001

Abstract

Sandwich beams, comprising a truss core and either solid or triangulated face-sheets, have been investment cast in an aluminium–silicon alloy and in silicon brass. The macroscopic effective stiffness and strength of the triangulated face-sheets and tetrahedral core are estimated by idealising them as pin-jointed assemblies; tests show that this approximation is adequate. Next, the collapse responses of these sandwich beams in 3-point bending are measured. Collapse is by four competing mechanisms: face-yield, face-wrinkling, indentation and core shear, with the active collapse mode dependent upon the beam geometry and yield strain of the material. Upper bound expressions for the collapse loads are given in terms of the effective properties of the faces and core of the sandwich beam; these upper bounds are in good agreement with the measured beam response, and are used to construct collapse mechanism maps with beam geometrical parameters as the axes. The maps are useful for selecting sandwich beams of minimum weight for a given structural load index. The optimisation reveals that truss core sandwich beams are significantly lighter than the competing concept of sandwich beams with a metallic foam core.

Keywords: Octet truss; Sandwich beams; Double layer grids; Plastic collapse; Optimal design

1. Introduction

Sandwich beams, comprising stiff and strong face-sheets and a low density core, are often used for weight efficient structures subjected to bending loads. Foam-cored sandwich panels compete with stringer-reinforced plates, particularly in curved configurations (Ashby et al., 2000), and a range of polymeric and metallic foams have been developed for such light weight structural applications. But it is possible to use materials which have greater stiffness to weight and strength to weight ratios than those of foams, by the following argument. The stiffness and strength of conventional random foams scales as $\bar{\rho}^2$ and $\bar{\rho}^{1.5}$, respectively, where $\bar{\rho}$ is the relative density of the foam (Ashby et al., 2000); these results are a direct consequence of the fact that the deformation mode of the microstructure is "bending-dominated" under all macroscopic stress states (Chen et al., 1999; Deshpande and Fleck, 2000). In contrast, the strength of a cellular metal scales as $\bar{\rho}$ when the cell walls deform predominantly by local stretching. It follows that a

* Corresponding author. Tel.: +44-1223-332-650; fax: +44-1223-332-662.
E-mail address: naf1@eng.cam.ac.uk (N.A. Fleck).

0020-7683/01/$ - see front matter
PII: S0020-7683(01)00103-2

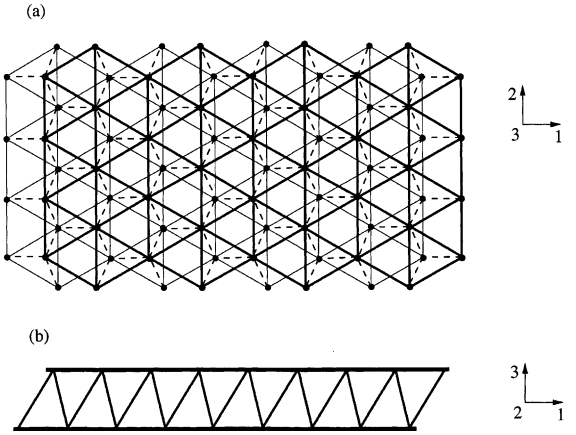

Fig. 1. (a) Top view of the octet-truss double layer grid. The bold and faint lines denote the triangulated lattice of the top and bottom layers while the dashed lines represent the tetrahedral core. (b) Side view of a sandwich beam with solid face-sheets and tetrahedral core; the core has an identical geometry to that of the octet-truss.

"stretching-dominated" microstructure is about 10 times stiffer and three times stronger than a bending-dominated microstructure for the choice $\bar{\rho} = 0.1$; and these ratios increase with diminishing $\bar{\rho}$.

Recently, Deshpande et al. (2001a) have analysed the topological criteria for cellular solids to be stretching-dominated. They considered a periodic assembly of pin-jointed struts with similarly situated nodes, and determined the degree of connectivity of bars per node in order to ensure rigidity. For the case of double layer grids they showed that a minimum of three core struts and six face-struts are needed at each node in order for stretching-dominated deformations to occur. A double layer grid satisfying this criterion is sketched in Fig. 1. They also considered a sandwich beam comprising solid face-sheets and a pin-jointed truss core; again, at least three core struts per node are required for collapse to occur by strut stretching.

In the present study we shall explore theoretically and experimentally the collapse response of stretching-dominated sandwich beams in 3-point bending. The beams have a tetrahedral truss core, and either solid or triangulated face-sheets, as sketched in Fig. 1. Parallel studies on similar sandwich beams have been completed recently by Wicks and Hutchinson (2001) and Wallach and Gibson (2001). Wicks and Hutchinson (2001) have conducted a comprehensive study on the optimal design of sandwich beams with a tetrahedral truss core and either solid or triangulated face-sheets. They found that the weight of the optimised beams for a given bending and shear strength was comparable to that for honeycomb-core sandwich beams and stringer-reinforced plates. Wallach and Gibson (2001) used experimental and finite element techniques to investigate the stiffness and strength of a double layer grid comprising triangulated faces and a pyramidal truss core. Analytical expressions for the stiffness and strength of a broad class of pyramidal and tetrahedral truss cores are derived below in the appendix.

The scope of this paper is as follows: first, we report on the manufacture of tetrahedral truss core sandwich beams with solid or triangulated face-sheets (as shown in Fig. 1). For the case of triangulated face-sheets the geometry of the double layer grid is that of Buckminster Fuller's octet truss (Fuller, 1961). Second, analytical formulae are derived for the effective elastic–plastic properties of the triangulated face-sheets and tetrahedral core. It is assumed that the macroscopic tensile strength is dictated by the yield of individual struts, whereas the macroscopic compressive strength is set by the competing modes of yield, elastic buckling and plastic buckling. These predictions are compared with measurements of the macroscopic stress versus strain response of double layer grids cast from LM25 aluminium–silicon alloy and MB1

silicon brass. Third, analytical expressions are given for the stiffness and strength of the sandwich beams in 3-point bending in terms of the effective properties of face-sheets and core. The predicted collapse loads for face-yield, face-wrinkling and core shear are compared with the measured values for selected beam geometries. And fourth, collapse mechanism maps are generated for sandwich beams in 3-point bending, with non-dimensional geometric parameters as axes. Such failure maps are used in determining minimum weight designs as a function of the appropriate structural load index.

2. Materials and manufacturing route

Sandwich beams were constructed using a tetrahedral core, and either solid face-sheets or triangulated face-sheets, as sketched in Fig. 1. The angle between the core struts and the faces was fixed at $\sin^{-1}(\sqrt{2/3})$, such that the strut-length of the core equalled that of the triangulated face-sheets. Two alloys were employed: an aluminium–silicon casting alloy LM25, of wt.% composition Al–Si 7–Mg 0.3, and a silicon brass MB1, of wt.% composition Cu–Si 4–Zn 14. The sandwich panels were investment cast from polystyrene pre-forms as follows: First, the tetrahedral cores and the triangulated face-sheets were injection moulded as separate pieces in polystyrene; [1] the cores were moulded with locating pins at the nodes, and the triangulated face-sheets were moulded with mating holes. Second, the polystyrene cores were solvent bonded to either triangulated or solid face sheets; and third, an investment casting process [2] was used to produce the LM25 and MB1 sandwich beams from the polystyrene sacrificial patterns. The tetrahedral core and triangulated face-sheets comprised solid circular cylinders of radius $a = 1$ mm and length $l = 14$ mm; the resulting double layer grids were of overall dimension $280 \times 130 \times 16$ mm^3. Photographs of the LM25 sandwich beams with both triangulated and 2 mm thick solid face-sheets are shown in Fig. 2.

3. Effective properties of the truss material

Before describing the sandwich beam response under 3-point loading, we begin by detailing calculations for the effective moduli and plastic collapse strengths of the triangulated face-sheets and the tetrahedral cores made from solid cylindrical struts of radius a and length l. Collapse by elastic and plastic buckling of the struts in the core and face-sheets is also addressed. These predictions are then compared with measurements on the LM25 and MB1 truss materials.

In the subsequent sandwich beam analysis it is assumed that the tensile and compressive stresses in the lower and upper face-sheets, respectively, balance the applied bending moment, with no contribution from bending of the core. On the other hand, the transverse shear and indentation loads are supported mainly by the core. Thus, the in-plane properties of the face-sheets and the out-of-plane properties of the tetrahedral core sandwiched between two rigid faces dictate the overall sandwich beam response under 3-point bending.

3.1. Elastic properties

The effective moduli of the sandwich beam are calculated upon assuming that the aspect ratio a/l of the struts is sufficiently small for the bending stiffness of the struts to be negligible compared to their stretching

[1] Meka Mouldings Ltd., 2nd Avenue, Edmonton, London, N18 2NW, UK 0181-807-5868.
[2] Micro Metalsmiths Ltd., Thornton Road Industrial Estate, Pickering, N. Yorks YO18 7JB, UK.

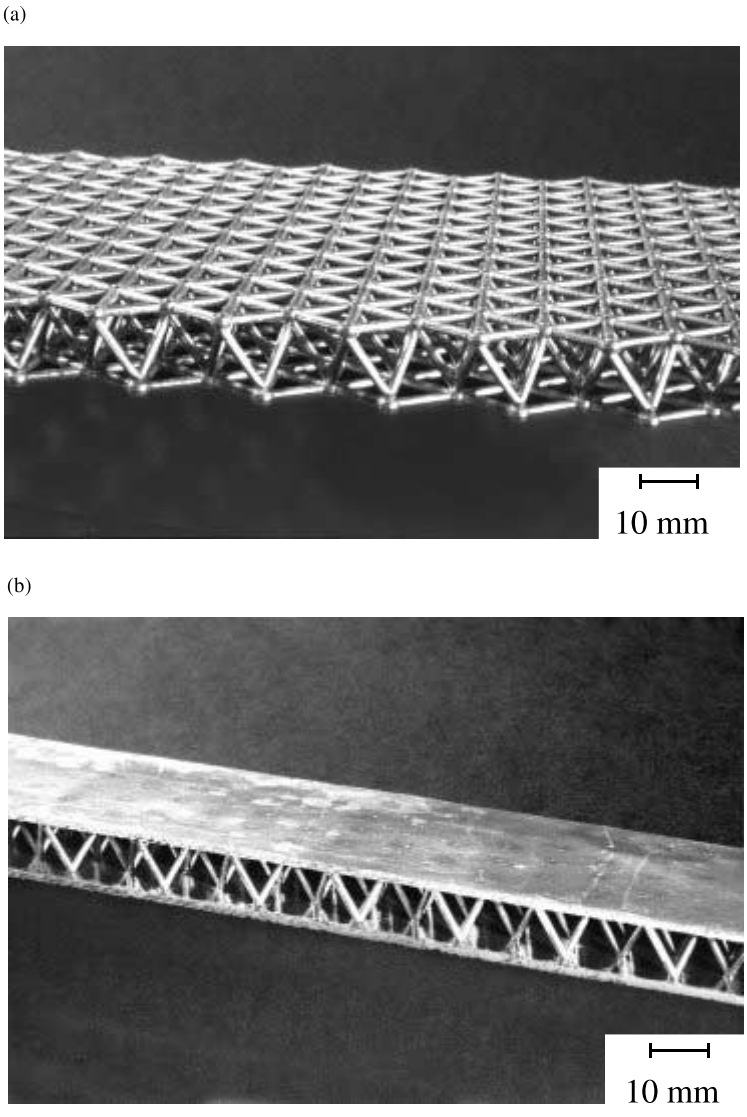

Fig. 2. Photographs of the LM25 truss core sandwich panels with (a) triangulated face-sheets and (b) solid face-sheets.

stiffness. Thus, the struts are assumed to be pin-jointed at the nodes, considerably simplifying the analysis given below.

3.1.1. Triangulated face-sheets

The elastic in-plane properties of the triangulated face-sheets are isotropic due to the 6-fold symmetry of the triangulated face-sheets about the 3-axis of Fig. 1. The effective Young's modulus and Poisson's ratio in the axes of Fig. 1 follow as (Hunt, 1993):

$$\frac{E_{11}^{f}}{E_s} = \frac{E_{22}^{f}}{E_s} = \frac{\pi}{\sqrt{3}}\left(\frac{a}{l}\right), \tag{1a}$$

and

$$v = \frac{1}{3}, \tag{1b}$$

where E_s is the Young's modulus of the strut material.

3.1.2. Tetrahedral core

Upon assuming that the struts of the tetrahedral core are bonded to the rigid faces by frictionless pin joints, the effective Young's modulus E_{33}^c and shear modulus G_{13}^c are given by:

$$\frac{E_{33}^c}{E_s} = \frac{4\sqrt{2}\pi}{3}\left(\frac{a}{l}\right)^2, \tag{2a}$$

and

$$\frac{G_{13}^c}{E_s} = \frac{\sqrt{2}\pi}{3}\left(\frac{a}{l}\right)^2, \tag{2b}$$

respectively.

3.2. Plastic collapse

In the upper bound calculations which follow for plastic collapse of the triangulated face-sheet and tetrahedral core it is assumed that the struts are pin-jointed and made from a rigid, ideally plastic solid. The macroscopic collapse stress is calculated by equating the external work to the plastic dissipation associated with stretching of the struts for kinematically-admissible modes of collapse. The symmetry of the truss materials is such that upper and lower bound collapse stresses coincide for each of the loading cases considered here. Thus, the collapse stresses cited below are exact results for the pin-jointed truss materials.

We begin by describing the collapse surface for (i) triangulated face-sheets in $(\sigma_{11}, \sigma_{22})$ space and (ii) a tetrahedral core sandwiched between rigid faces in $(\sigma_{33}, \sigma_{13})$ space, using the reference frame of Fig. 1.

3.2.1. Collapse surface of triangulated face-sheets in (σ_{11}, σ_{22}) space

Postulated collapse modes for the triangulated face-sheets under the macroscopic stress state $(\sigma_{11}, \sigma_{22})$ are sketched in top views of the triangular cells in Fig. 3. In these sketches, the solid straight lines denote struts in the rigid state, and the dashed lines refer to struts that are actively yielding. The struts yield in either compression or tension (as denoted by arrows in Fig. 3) and thus two collapse locii exist for each collapse mode. For the collapse Mode I, the strut labelled n1–n2 (so designated because it lays between nodes n1 and n2) dissipates plastic work and the associated segments of the yield surface are given by

$$\text{Mode Ia}: \quad \frac{\sigma_{22}}{\sigma_Y} = \frac{\sigma_{11}}{3\sigma_Y} - \frac{\pi}{\sqrt{3}}\left(\frac{a}{l}\right), \tag{3a}$$

and

$$\text{Mode Ib}: \quad \frac{\sigma_{22}}{\sigma_Y} = \frac{\sigma_{11}}{3\sigma_Y} + \frac{\pi}{\sqrt{3}}\left(\frac{a}{l}\right), \tag{3b}$$

where σ_Y is the yield stress of the solid material. For Mode II, the struts n1-n3 and n2-n3 dissipate plastic work and the collapse planes become

$$\text{Mode IIa}: \quad \frac{\sigma_{11}}{\sigma_Y} = -\frac{\sqrt{3}\pi}{2}\left(\frac{a}{l}\right), \tag{4a}$$

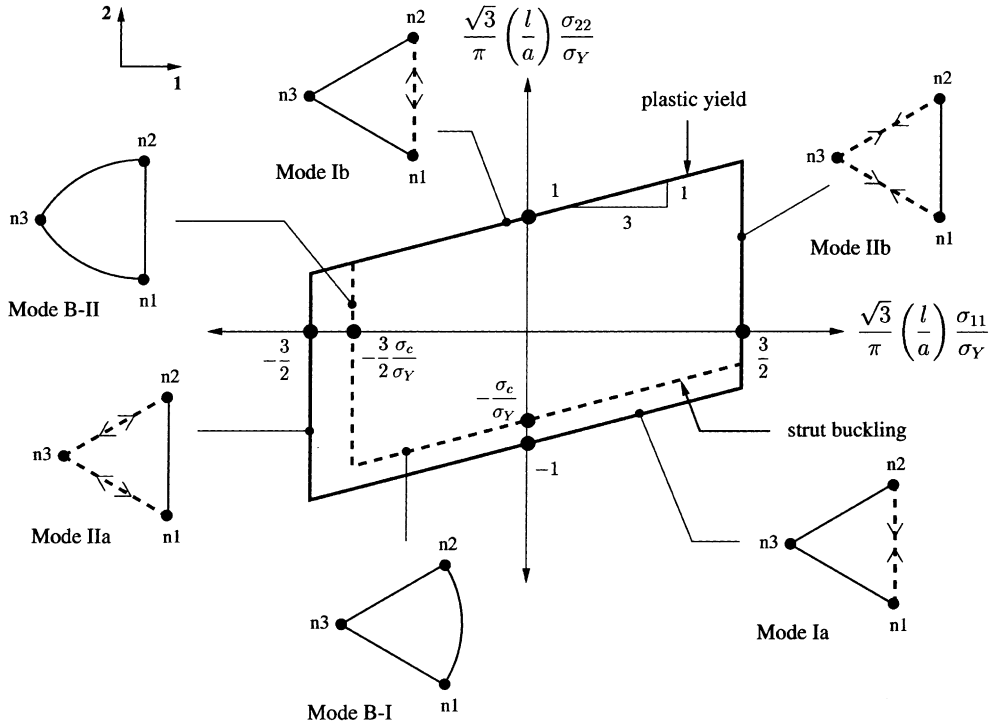

Fig. 3. Collapse surface of the triangulated face-sheets in $(\sigma_{11}, \sigma_{22})$ space. In the sketches of the collapse modes, the solid lines represent struts in the rigid state, the straight dashed lines represent struts undergoing plastic collapse and the curved solid lines represent buckling struts.

and

$$\text{Mode IIb}: \quad \frac{\sigma_{11}}{\sigma_Y} = \frac{\sqrt{3}\pi}{2}\left(\frac{a}{l}\right). \tag{4b}$$

3.2.2. Collapse surface of the tetrahedral core sandwiched between rigid faces in $(\sigma_{33}, \sigma_{13})$ space

Deshpande et al. (2001b) have previously explored the collapse modes for a tetrahedral core under combinations of applied stress $(\sigma_{33}, \sigma_{13})$; the collapse locus and the associated collapse modes are sketched in plan views of the tetrahedral cell in Fig. 4. Again, dashed straight lines and solid lines denote struts undergoing active yield and in the rigid state, respectively, while a solid circle represents rotation at a frictionless joint. In Mode I, the two struts p2-p4 and p3-p4 dissipate work while in Mode II the strut p1-p4 yields. The collapse locii are

$$\text{Mode Ia}: \quad \frac{\sigma_{13}}{\sigma_Y} = \frac{\sigma_{33}}{\sqrt{2}\sigma_Y} + 2\pi\left(\frac{a}{l}\right)^2, \tag{5a}$$

and

$$\text{Mode Ib}: \quad \frac{\sigma_{13}}{\sigma_Y} = \frac{\sigma_{33}}{\sqrt{2}\sigma_Y} - 2\pi\left(\frac{a}{l}\right)^2 \tag{5b}$$

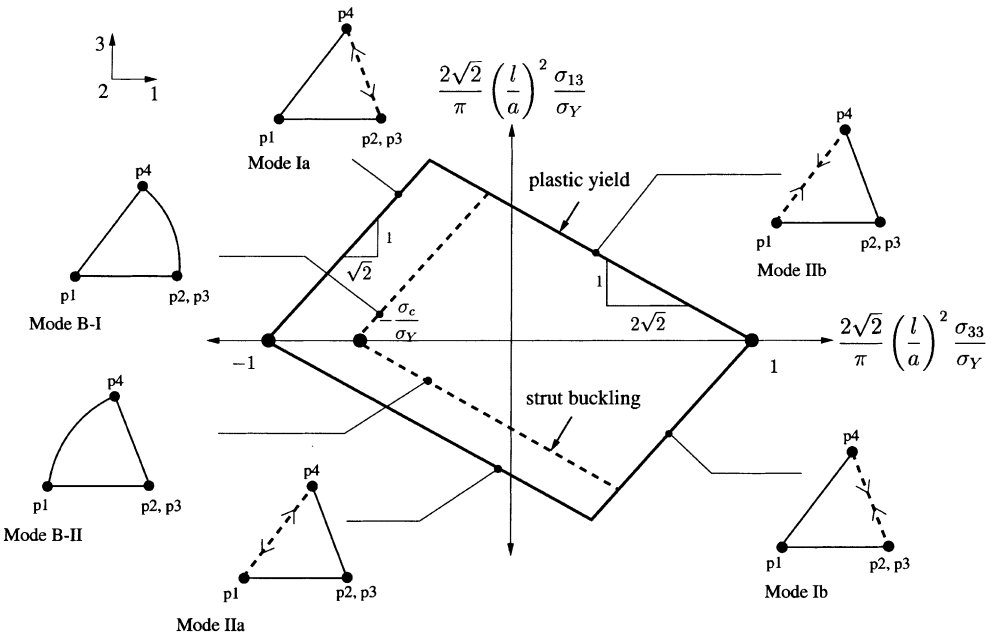

Fig. 4. Collapse surface of the tetrahedral core in $(\sigma_{33}, \sigma_{13})$ space. In the sketches of the collapse modes, the solid lines represent struts in the rigid state, the straight dashed lines represent struts undergoing plastic collapse and the curved solid lines represent buckling struts.

for Mode I and

$$\text{Mode IIa}: \quad \frac{\sigma_{13}}{\sigma_Y} = -\frac{\sigma_{33}}{2\sqrt{2}\sigma_Y} - \pi\left(\frac{a}{l}\right)^2, \tag{6a}$$

and

$$\text{Mode IIb}: \quad \frac{\sigma_{13}}{\sigma_Y} = -\frac{\sigma_{33}}{2\sqrt{2}\sigma_Y} + \pi\left(\frac{a}{l}\right)^2 \tag{6b}$$

for Mode II. Under uniaxial compression σ_{33}, the tetrahedra collapse independently with zero transverse straining. Consequently, the indentation strength of the tetrahedral truss core is approximately equal to its uniaxial compressive strength, σ_{33}^{cY}.

3.3. Elastic and plastic buckling of the triangulated face-sheets and tetrahedral core

The sandwich beams may collapse by the local elastic or plastic buckling of the constituent struts. Recall that the axial bifurcation strength of a solid circular cylindrical strut of radius a and length l is given by the Shanley tangent-modulus buckling formula

$$\sigma_c = \frac{k^2\pi^2 E_t a^2}{4l^2}, \tag{7}$$

where E_t is the tangent-modulus, defined by the slope $d\sigma/d\epsilon$ of the uniaxial stress versus strain curve of the solid material at the stress level σ_c. The factor k in Eq. (7) depends upon the rotational stiffness of the end nodes of the strut and is central to the problem of calculating σ_c for a given network of struts. When a strut

buckles, the rotation of its ends is opposed by the bending stiffness of the other struts: they exert a restoring moment and it is this that determines the factor k^2 in Eq. (7). Thus, k depends upon the buckling mode. The cells of the truss materials may buckle in many different modes and the resulting problem is difficult to analyse completely. However, upper and lower limits on the buckling stress are obtained by taking $k = 1$ and 2 corresponding to pin-jointed and fully clamped end conditions, respectively.

The tangent modulus E_t depends upon the strain hardening characteristics of the strut material. For an elastic, ideally plastic solid, E_t equals the Young's modulus E_s of the solid material and Eq. (7) reduces to the Euler buckling stress; such struts will buckle elastically when the yield strain ϵ_Y exceeds $((\pi ka)/2l)^2$ but will yield for smaller values of ϵ_Y. The stress versus strain response of a strain hardening solid is commonly described by the Ramberg–Osgood relation

$$\frac{\epsilon}{\epsilon_Y} = \frac{\sigma}{\sigma_Y} + \frac{3}{7}\left(\frac{\sigma}{\sigma_Y}\right)^n, \tag{8}$$

where $\sigma_Y \equiv E_s\epsilon_Y$ is the representative yield strength of the solid, and n is the strain hardening exponent. For such a material description, the bifurcation stress σ_c is given by the implicit relation

$$\left(\frac{\pi ka}{2l}\right)^2 \epsilon_Y^{-1} = \left(\frac{\sigma_c}{\sigma_Y}\right) + \frac{3}{7}n\left(\frac{\sigma_c}{\sigma_Y}\right)^n \tag{9}$$

from Eq. (7). The macroscopic collapse stresses associated with strut-buckling are estimated by a simple work calculation in which the external work increment is equated to the internal work increment associated with buckling of the struts for a kinematically admissible collapse mode. The collapse stress is derived in terms of the local buckling stress σ_c of the struts, where σ_c is given by the solution of Eq. (9) for a Ramberg–Osgood solid. We assume infinitesimal straining, and write the virtual work expression in terms of the initial configuration; consequently these estimates of strength become inaccurate when large deformations occur prior to the onset of buckling. We proceed by exploring the effect of strut buckling upon the macroscopic collapse surfaces for the triangulated face-sheets and tetrahedral core.

3.3.1. Collapse surface of the triangulated face-sheets in (σ_{11}, σ_{22}) space with strut buckling active

The effect of strut buckling upon the collapse response of the triangulated faces under macroscopic $(\sigma_{11}, \sigma_{22})$ loading is sketched in Fig. 3, upon assuming $\sigma_c < \sigma_Y$. The possible buckling modes are shown in top views of the triangular cell, with the curved solid lines representing the buckled struts. Since the struts only buckle in compression, a single collapse plane is associated with each buckled state, and is given by

$$\text{Mode B-I}: \quad \frac{\sigma_{22}}{\sigma_c} = \frac{\sigma_{11}}{3\sigma_c} - \frac{\pi}{\sqrt{3}}\left(\frac{a}{l}\right), \tag{10a}$$

and

$$\text{Mode B-II}: \quad \frac{\sigma_{11}}{\sigma_c} = -\frac{\sqrt{3}\pi}{2}\left(\frac{a}{l}\right). \tag{10b}$$

3.3.2. Collapse surface of the tetrahedral core sandwiched between rigid faces in (σ_{33}, σ_{13}) space with strut buckling active

Now consider the effect of strut buckling upon the collapse of the tetrahedral core under stress states $(\sigma_{33}, \sigma_{13})$. Provided that σ_c is less than σ_Y, the collapse surface for strut buckling lies inside that for plastic yield, as sketched in Fig. 4. The collapse modes are displayed in side views of the tetrahedral cell in the figure, with curved solid lines again representing buckled struts. The collapse locii are given by

$$\text{Mode B-I}: \quad \frac{\sigma_{13}}{\sigma_c} = \frac{\sigma_{33}}{\sqrt{2}\sigma_c} + 2\pi\left(\frac{a}{l}\right)^2, \tag{11a}$$

and

$$\text{Mode B-II}: \quad \frac{\sigma_{13}}{\sigma_c} = -\frac{\sigma_{33}}{2\sqrt{2}\sigma_c} - \pi\left(\frac{a}{l}\right)^2. \tag{11b}$$

3.4. Comparison of predicted and measured effective properties

We proceed by comparing the analytical predictions of the effective properties of the triangulated face-sheets and the tetrahedral truss cores with measured values for both the LM25 and MB1 alloys.

3.4.1. Material properties of the constituent struts

In order to compare the measured and predicted stiffness and strength of the truss materials, we first measured the uniaxial tensile response of the as-cast LM25 and MB1 alloys. Tensile specimens of dog-bone geometry were cut from the in-gates of the investment castings. The measured Cauchy stress versus logarithmic strain curves are plotted in Fig. 5 for a strain rate of 10^{-3} s^{-1}. We conclude that the LM25 aluminium silicon alloy can be approximated as an elastic, ideally plastic solid with a Young's modulus $E_s = 70$ GPa and a yield strength $\sigma_Y = 170$ MPa. In contrast, the MB1 silicon brass displays high strain hardening, and the uniaxial stress versus strain curve is adequately fitted by the Ramberg–Osgood equation (8) with $n = 4$, $\sigma_Y = 100$ MPa and $\epsilon_Y = 0.1\%$.

3.4.2. Tensile tests on triangulated face-sheets

Tensile tests in the 1-direction were conducted on LM25 and MB1 dogbone shaped triangulated face-sheet specimens of gauge length 190 mm and width 85 mm; since the strut length l equals 14 mm the gauge section is of dimension 29 by 13 cells. We note in passing that these dogbone specimens display no edge effects: for a pin-jointed structure of this geometry the bar tensions do not vary across the width of the specimen. These specimens were cast with the locating holes infilled, in order to mimic the strengthening due to the presence of the pins of the tetrahedral core. A clip gauge of length 50 mm and spanning approximately four cells was used to monitor the axial strain while the load was measured by the load cell of the test machine and used to define the nominal axial stress on the net section of the specimen.

Under uniaxial tension in the 1-direction, the LM25 face-sheet exhibits an initial linear elastic behaviour, followed by a hardening response and terminated by strut fracture at a macroscopic axial strain of 1.8%, see Fig. 6a. The analytical predictions of modulus E_{11}^f and strength σ_{11}^{fY} (Eqs. (1a) and (4b), respectively), are included in Fig. 6a, and are in good agreement with the measurements.

The measured macroscopic stress versus strain response of the MB1 face-sheet is shown in Fig. 6b. As for the LM25 alloy, the MB1 triangulated face-sheet exhibits an initial linear elastic behaviour followed by a hardening response. However, the MB1 face-sheet is more ductile than the LM25 face-sheet and has a nominal fracture strain of about 10%. Two predictions of the stress–strain response of the triangulated face-sheet are given in Fig. 6b:

(i) An infinitesimal calculation for an elastic, ideally plastic solid, with a measured modulus $E_S = 100$ GPa and an ultimate tensile strength $\sigma_{UTS} = 465$ MPa.
(ii) A finite deformation calculation, allowing for a finite rotation of the nodes during axial extension of the triangulated face-sheet. The calculation also makes use of the measured stress versus strain curve of the MB1 alloy, as given in Fig. 5b.

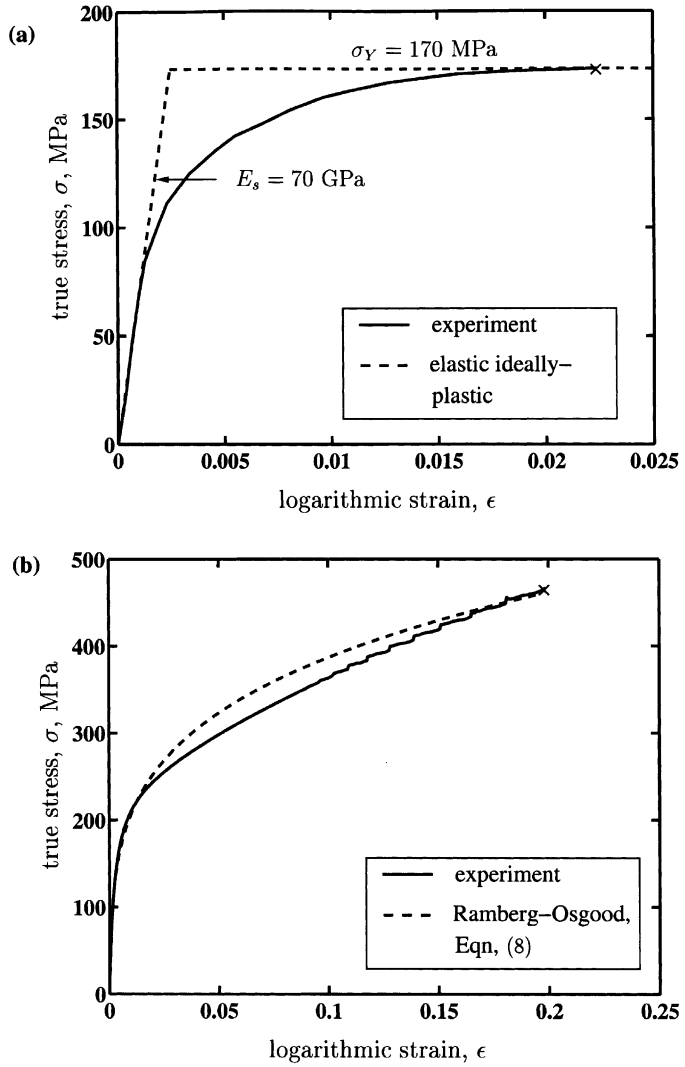

Fig. 5. Measured tensile stress versus strain curve of the as-cast alloys shown as solid lines, and idealised responses shown as dotted lines. (a) LM25 alloy, with elastic–ideally plastic representation. (b) MB1 alloy with Ramberg–Osgood representation (8), with the choice $n = 4$, $\sigma_Y = 100$ MPa and $\epsilon_Y = 0.1\%$.

Method (i) grossly overpredicts and method (ii) moderately overpredicts the measured σ_{11} versus ϵ_{11} curve for the triangulated MB1 face-sheets; although method (ii) captures the initial response, it does not account for the premature failure of the face-sheets due to the presence of strain concentrations within individual struts adjacent to the nodes.

3.4.3. Normal compression of tetrahedral core sandwiched between rigid faces

Compression tests in the 3-direction of Fig. 1 were conducted on the LM25 and MB1 tetrahedral truss cores sandwiched between 2 mm thick solid face-sheets. The solid face-sheets were cast integrally with the tetrahedral core, and were sufficiently stiff to be treated as rigid in comparison to the truss core. The

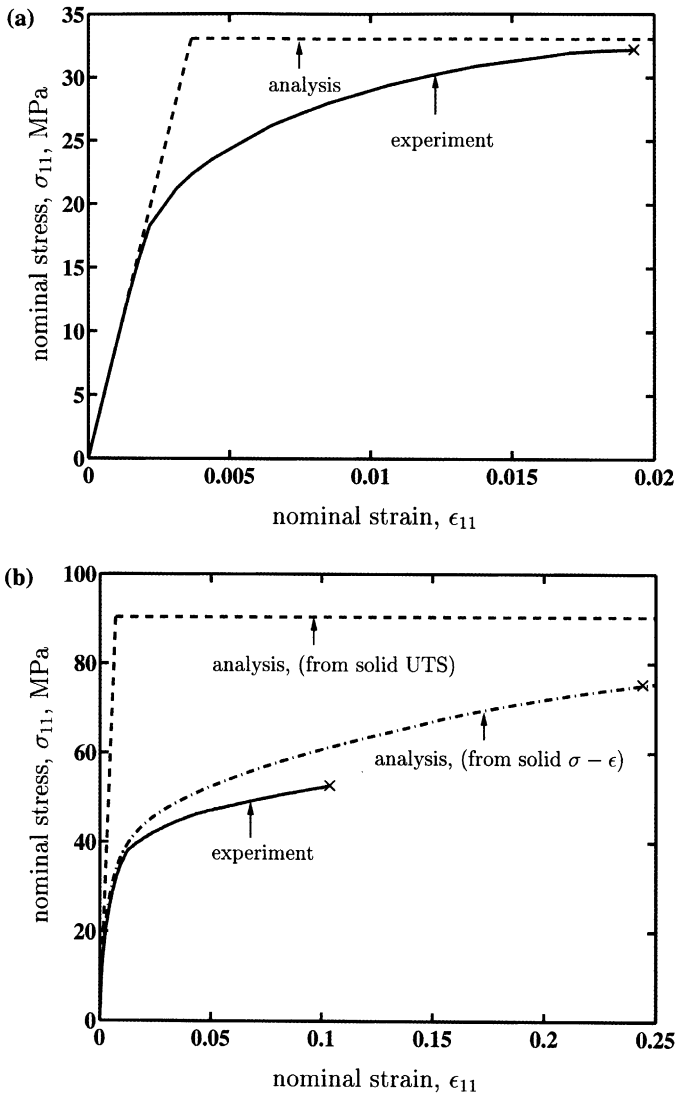

Fig. 6. Measured tensile stress versus strain response (σ_{11} versus ϵ_{11}) of triangulated face-sheets made from (a) LM25 and (b) MB1. The dotted lines are analytical predictions of the elastic–ideally plastic response, assuming infinitesimal straining, while the chain-dotted lines for the MB1 alloy denote the finite deformation analysis making use of the Ramberg–Osgood material description (8) with the choice $n = 4$, $\sigma_Y = 100$ MPa and $\epsilon_Y = 0.1\%$.

compression tests were performed using a standard screw driven test machine at a nominal strain rate of 10^{-3} s^{-1}. The applied load was measured by the load cell of the test machine and was used to define the nominal stress in the specimen; the nominal axial strain was measured via a clip gauge fixed between the solid face-sheets.

The measured uniaxial stress versus strain curve, σ_{33} versus ϵ_{33}, for the LM25 material is plotted in Fig. 7a. The stress versus strain curve exhibits a hardening response up to a strain of approximately 5%, with the peak strength set by plastic collapse. Beyond this strain, the response is softening due to plastic buckling of

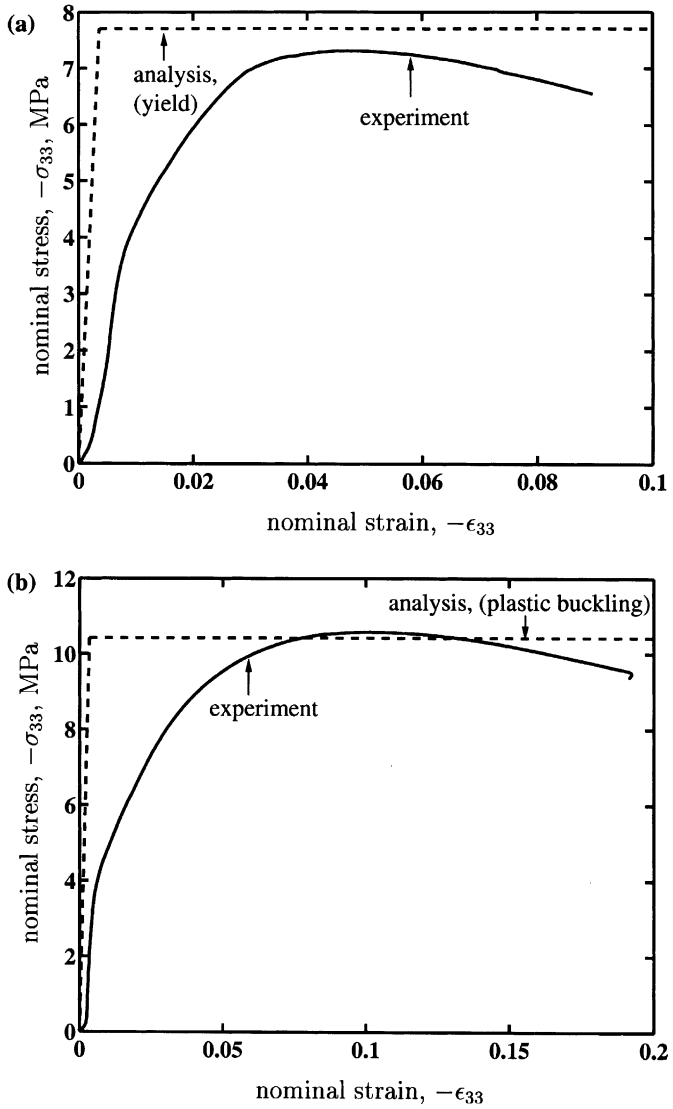

Fig. 7. Uniaxial compressive stress versus strain curves (σ_{33} versus ϵ_{33}) of the tetrahedral truss core, sandwiched between solid face-sheets of thickness 2 mm, for (a) LM25 and (b) MB1 alloys. The dotted line in (a) represents the elastic–ideally plastic collapse prediction, while the dotted line in (b) represents the elastic–plastic buckling prediction.

the struts. Bedding-in effects during the early stages of deformation are apparent in Fig. 7a. These bedding-in effects occur at the attachment points of the tetrahedral truss core to the face-sheets with the pins of the tetrahedral core bedding into the solid faces during the initial stages of deformation. The analytical prediction of strength (Eq. (5a)) is shown in Fig. 7a and is in good agreement with the measures strength. On the other hand, the predicted modulus (2a) exceeds the measured value due to bedding-in effects at the joints.

The measured σ_{33} versus ϵ_{33} response of the MB1 truss core is shown in Fig. 7b; a hardening behaviour is observed up to a strain of about 10%, followed by softening due to plastic buckling of the struts. In contrast

to the LM25 truss core which collapses by plastic yield, the compressive strength σ_{33}^{cY} of the MB1 core is controlled by plastic buckling of the struts. The critical buckling stress σ_c of the MB1 struts is given by Eq. (9) and is a function of the strut aspect ratio a/l, the Ramberg–Osgood material parameters σ_Y, ϵ_Y and n, and the end-constraints on the struts which determine the value of k. Visual examination of the deformed MB1 specimens revealed that the buckling mode of the struts corresponds to fully clamped end-constraints, implying the value $k = 2$. The strength as given by Eq. (11a) (with $k = 2$) is plotted in Fig. 7b and agrees well with the experimental measurements. We note in passing that the buckling stress σ_c calculated using Eq. (9) is only about 5% higher than that calculated numerically using the measured uniaxial stress versus strain curve of the MB1 alloy.

3.4.4. Shear tests on the tetrahedral core

The shear response, σ_{13} versus ϵ_{13}, of the tetrahedral core sandwiched between 2 mm thick solid faces was measured using the single-lap shear configuration in accordance with the ASTM Standard C273-94 (1994). Specimens of dimension $170 \times 65 \times 16$ mm^3 were fastened to steel plates using self-tapping screws and were then subjected to shear loading with the load line along one diagonal. The sign of σ_{13} was dependent upon the orientation of the specimens in the steel grips. The applied load was measured by the load cell of the test machine, while a clip gauge was used to measure the relative sliding displacement of the steel plates and thereby the average shear strain in the specimen.

The σ_{13} versus ϵ_{13} responses of the LM25 truss core are symmetric about the origin to within experimental error, see Fig. 8a. Failure is by the shearing of the pins of the tetrahedral truss core at the joints with the face-sheets, at an average shear strain of about 3%. The predicted shear strength of the core due to shearing of these pins is given by

$$\sigma_{13}^{cY} = \frac{2\pi}{\sqrt{3}} \left(\frac{a}{l}\right)^2 \tau_Y, \tag{12}$$

where τ_Y is the shear strength of the alloy, and a is the radius of the pin (equal to that of the struts). For simplicity we assume that the shear strength τ_Y is given by the Tresca relation $\tau_Y = \sigma_Y/2$. The strength prediction, Eq. (12), is plotted in Fig. 8a and is in good agreement with the experimental measurements. In contrast, the strength estimate from the strut stretching analysis (Eq. (5a)) overestimates the measured values. The prediction (2b) of the shear modulus also overpredicts the measured value due to the occurrence of additional shear and bending deflections of the pins at the attachment points between the tetrahedral core and the face-sheets; this is a consequence of the fact that the centre lines of the core struts meet on a plane within the core and not at mid-thickness of the face-sheets.

Next, consider the shear response of the MB1 truss core. As for the LM25 case, the responses are identical in the positive and negative 1–3 directions to within experimental error, see Fig. 8b. Shear failure is again by shearing of the pins of the tetrahedral truss core, with the prediction (12) in good agreement with the measured peak stress (where we have taken the shear strength of the solid MB1 to be $\tau_Y = \sigma_{UTS}/2$). The predictions of the strut-stretching analyses are included in Fig. 8b. The predicted collapse strength in the negative 1–3 direction due to the plastic buckling of the struts (Mode BII with $k = 2$) is approximately equal to that due to pin-shear; visual inspection of the failed specimens confirmed that both shearing of the pins and plastic buckling of the struts had occurred. In the positive 1–3 direction, the predicted collapse strength due to the plastic buckling of the struts (Mode BI with $k = 2$) is approximately equal to that due to plastic yielding of the struts (Mode IIb) at the ultimate tensile strength, σ_{UTS} of the solid MB1. However, the Mode BI and IIb collapse strengths are much greater than the pin shearing collapse strength; this prediction is confirmed by no visual evidence of plastic buckling of the tetrahedral truss core struts.

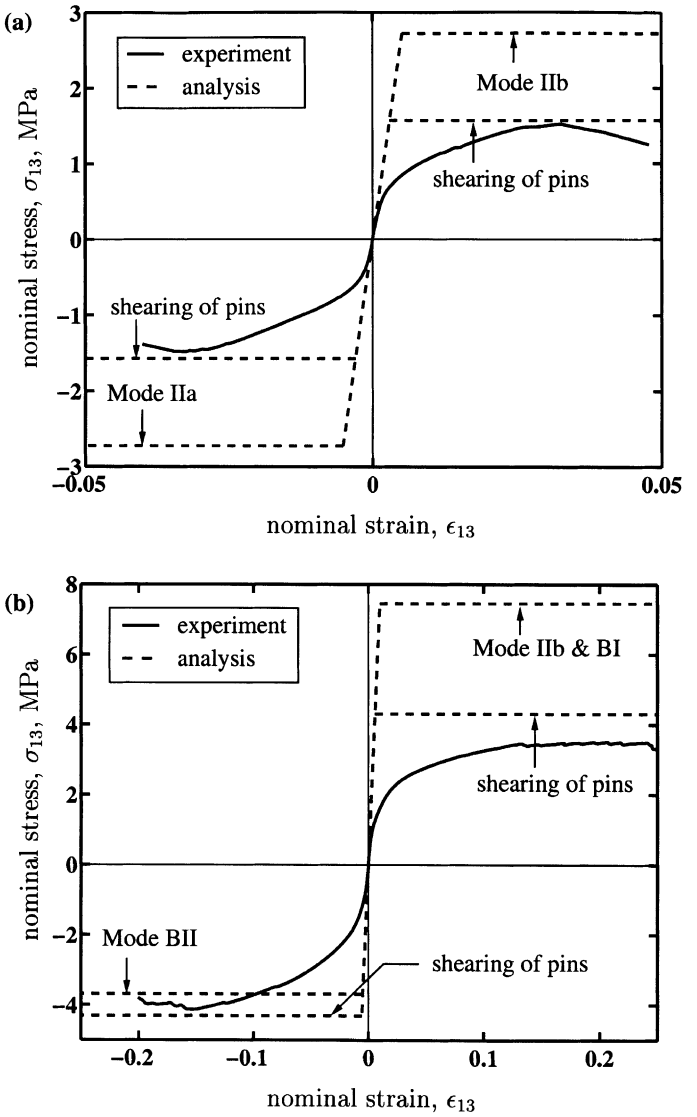

Fig. 8. Shear stress versus strain (σ_{13} versus ϵ_{13}) responses of the tetrahedral truss core in the positive and negative 1–3 directions. (a) LM25 truss core, (b) MB1 truss core. The dotted lines are analytical predictions of the shear modulus and collapse strength.

4. Prediction of stiffness and strength of truss beams in 3-point bending

In this section we cite analytical formulae for the stiffness and collapse strengths of truss-core sandwich beams in three point bend, with the geometry as sketched in Fig. 9a. The sandwich beams are oriented such that loading is parallel to the 2-axis as defined in Fig. 1. We assume that both the core and face-sheets are elastic–ideally plastic continua; the appropriate effective properties of the core and face-sheets are derived in Section 3. Consider a sandwich beam of uniform width b, comprising two identical face-sheets of thickness t perfectly bonded to a truss core of thickness c. The beam is loaded in 3-point bending by circular cylindrical

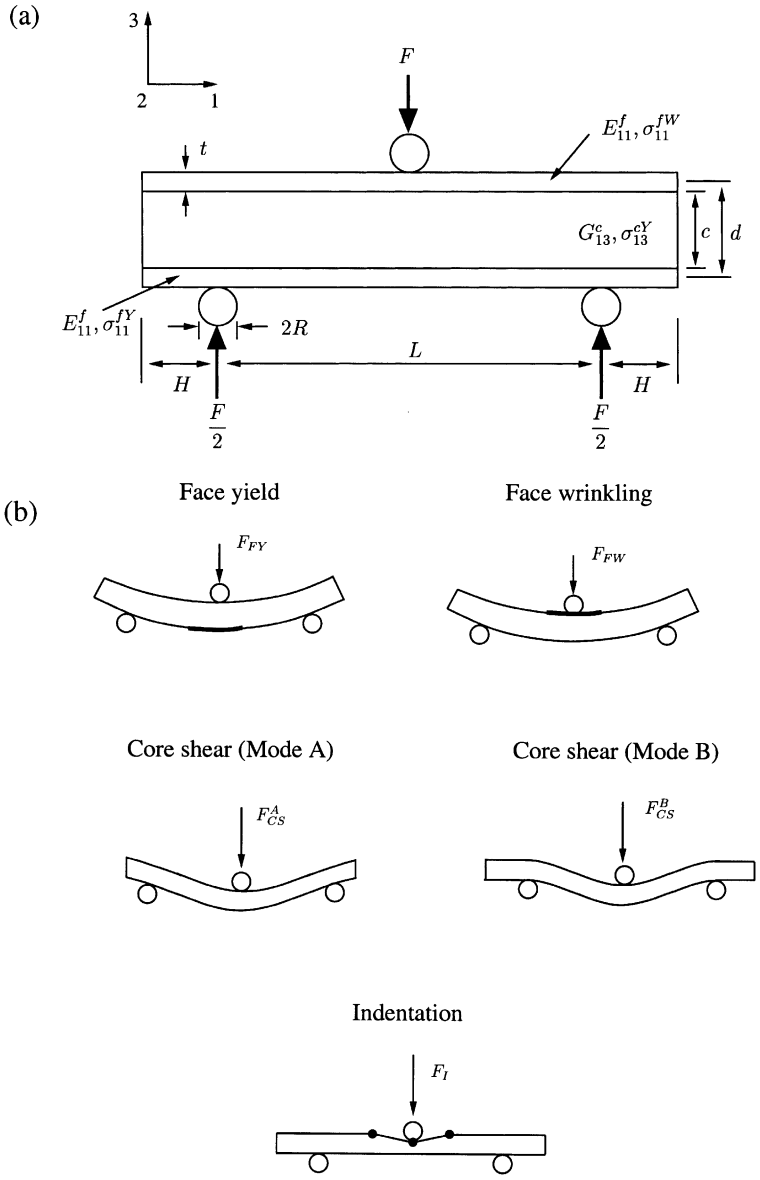

Fig. 9. (a) A sandwich beam under 3-point bend loading. (b) Collapse modes of a sandwich beam under 3-point bend loading.

rollers of radius R, see Fig. 9a. The span between the outer supports is L and the overhang distance beyond the outer supports is H.

4.1. Analytical predictions of stiffness

The relative elastic deflection δ of the inner and outer rollers is the sum of the flexural and shear deflections (see, Allen (1969)),

$$\delta = \frac{FL^3}{48(EI)_{eq}} + \frac{FL}{4(AG)_{eq}}, \tag{13a}$$

where the equivalent flexural rigidity $(EI)_{eq}$ is

$$(EI)_{eq} = \frac{E_{11}^f btd^2}{2} + \frac{E_{11}^f bt^3}{6} \approx \frac{E_{11}^f btd^2}{2}, \tag{13b}$$

in terms of the Young's modulus E_{11}^f of the face-sheets in the 1-direction as defined in Figs. 1 and 9a. Typically, the core gives a negligible contribution to the overall bending stiffness. The equivalent shear rigidity $(AG)_{eq}$ is dictated by the shear stiffness of the core, and is given by

$$(AG)_{eq} = \frac{bd^2}{c} G_{13}^c \approx bcG_{13}^c \tag{13c}$$

in terms of out-of-plane the shear modulus G_{13}^c of the tetrahedral core in the 1–3 direction, the cross-sectional area A of the core and the spacing $d = c + t$ of the mid-planes of the face-sheets.

4.2. Collapse modes: limit load calculations

Ashby et al. (2000) calculated upper bound loads for the competing collapse modes of a sandwich beam by idealising the core and face-sheets as rigid, ideally plastic solids, see Fig. 9b. Analytical formulae for the collapse strengths of truss-core sandwich beams in 3-point bending are now stated in terms of the appropriate effective strengths of the face-sheets and the tetrahedral core; full details are given in Ashby et al. (2000).

4.2.1. Face yield

At any given value of applied load, the maximum bending moment on the beam cross-section is attained at the location of the central roller. Plastic collapse occurs when this maximum bending moment attains the collapse moment for the beam cross-section, and corresponds to the condition that the face-sheets attain the yield strength σ_{11}^{fY} in the 1-direction. The collapse load F_{FY} is then given by

$$F_{FY} = \frac{4bt(c+t)}{L} \sigma_{11}^{fY}, \tag{14}$$

where we have neglected the contribution to collapse load associated with plastic bending of the core.

4.2.2. Face wrinkling

The upper face-sheets are subjected to compressive stresses and, at the location of maximum bending moment on the beam cross-section (beneath the central roller), they may fail by elastic or plastic buckling instead of plastic collapse. The critical wrinkling stress of the face-sheets in the 1-direction, σ_{11}^{fW}, depends upon the buckling mode including the inter-nodal distance of the tetrahedral core, as detailed in Section 3.3.1. The collapse load F_{FW} of the truss beam is given by the analogous expression to Eq. (14), viz

$$F_{FW} = \frac{4bt(c+t)}{L} \sigma_{11}^{fW}. \tag{15}$$

4.2.3. Core shear

The transverse shear force exerted on a sandwich beam in 3-point bending is carried mainly by the core; consequently, plastic collapse by core shear can occur. Ashby et al. (2000) identified two competing modes of core shear. Mode A entails core shear over the full length $(L + 2H)$ of the sandwich beam, with plastic hinge formation in both face-sheets beneath the central roller. Mode B comprises core shear over the

central portion of length L, with plastic hinge formation in both face-sheets at the outer loading points; thus, the overhanging regions of the sandwich beam, located beyond the outer supports, remain rigid. The collapse loads by Modes A and B are given by

$$F_{CS}^{A} = 2\frac{bt^2}{L}\sigma_{11}^{fY} + 2bc\sigma_{13}^{cY}\left(1 + \frac{2H}{L}\right) \tag{16a}$$

and

$$F_{CS}^{B} = 4\frac{bt^2}{L}\sigma_{11}^{fY} + 2bc\sigma_{13}^{cY}, \tag{16b}$$

respectively. Here, σ_{13}^{cY} is the shear strength of the tetrahedral core in the 1–3 direction. Note that collapse Mode A is activated for small lengths of overhang H, and the collapse mechanism is expected to switch to Mode B for overhangs satisfying the relation

$$H > \frac{1}{2}\frac{t^2}{c}\frac{\sigma_{11}^{fY}}{\sigma_{13}^{cY}}. \tag{17}$$

4.2.4. Indentation

The indentation mode of collapse involves the formation of three plastic hinges within the top face-sheet adjacent to the central indenter, with compressive yield of the underlying core. The indentation pressure of the tetrahedral core is assumed to equal its uniaxial compressive strength; supporting arguments for this are given in Section 3.2.2. Both upper and lower bound analyses by Ashby et al. (2000) indicate that the indentation load F_I is given by

$$F_I = 2bt\sqrt{\sigma_{11}^{fY}\sigma_{33}^{cY}}, \tag{18}$$

where σ_{33}^{cY} is the uniaxial compressive strength of the core in the 3-direction.

5. Three-point bend tests on sandwich beams

The sandwich beams were loaded in 3-point bend by 19 mm diameter cylindrical rollers aligned parallel to the 2-direction of Fig. 1. The central roller was displaced at a rate of 0.02 mm s^{-1} and the applied load and central roller displacement were recorded. To gain insight into the collapse mechanisms, the beams were instrumented as shown schematically in Fig. 10. A clip gauge (CG) was used to measure the change in height of the beam directly under the central roller and two additional clip gauges were used to measure the relative sliding of the face-sheets on each side of the central roller, and thereby the average shear strain in the core. Additionally, 120 Ω strain gauges (SG) of length 1 mm were placed at mid-span on the lower face-sheet. The beams with triangulated face-sheets had the strain gauges fixed onto struts parallel and inclined to the axis of the rollers, as shown schematically in Fig. 10b, while a 90° rosette measuring longitudinal and transverse strains was used for the beams with solid face-sheets.

Ideally, we would have wished to have designed specimen geometries in order to probe the regimes of dominance of the competing collapse modes of face yield, face wrinkling, core shear and indentation. However, in the current study the strut radius and length were fixed at 1 and 14 mm, respectively, as it was not feasible to make a range of injection moulding tools to manufacture polystyrene precursor templates with different strut dimensions. Further, limitations with current investment castings capabilities restricted us to 2 mm thick solid face-sheets; thinner face-sheets resulted in "misrun failures". The geometries considered are summarised in Table 1: the span L was varied while keeping the overhang H a constant. In the

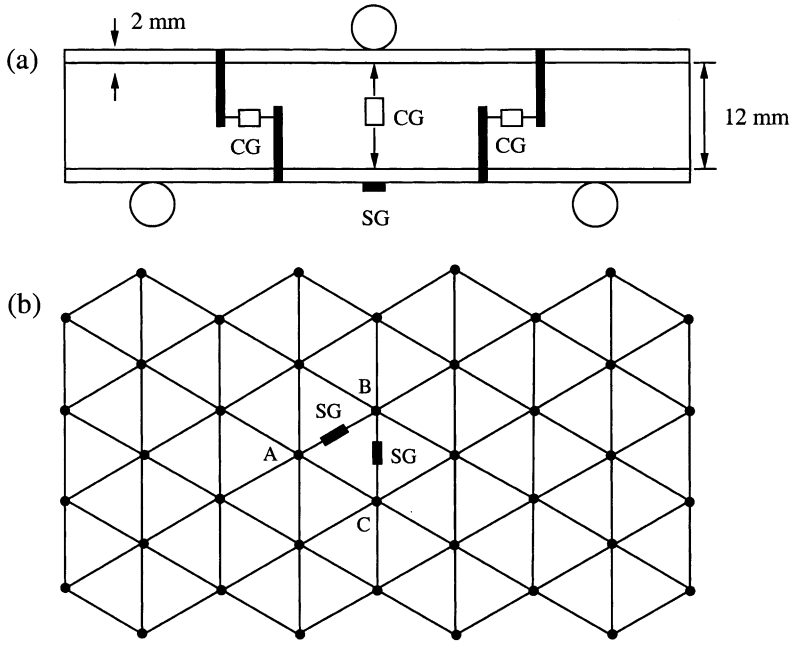

Fig. 10. (a) Location of clip gauges and strain gauges on the truss core sandwich beams loaded in three-point bend. (b) Sketch showing the locations of the strain gauges on the lower triangulated face-sheet.

Table 1
Geometry of the three point bend specimens[a]

	Specimen	Material	Width, b (mm)	Span, L (mm)
Triangulated face-sheets	L1	LM25	130	110
	L2	LM25	130	190
	M1	MB1	130	110
	M2	MB1	130	190
Solid face-sheets, $t = 2$ mm	L3	LM25	65	110
	L4	LM25	65	190
	M3	MB1	65	110
	M4	MB1	65	190

[a] In all cases, the strut aspect ratio $a/l = 0.071$, the core thickness $c = 12$ mm and the overhang $H = 45$ mm.

remainder of this section the measured collapse responses of the LM25 and MB1 sandwich beams with triangulated and solid face-sheets are compared with the analytic predictions.

5.1. Sandwich beams with triangulated face-sheets

The observed collapse mode of the LM25 sandwich beams with triangulated faces (designated L1 and L2 in Table 1) was face yield with the struts on the lower face-sheets yielding in tension. On the other hand, the collapse mode of the MB1 beams (labelled M1 and M2 in Table 1) was face wrinkling due to plastic buckling of the struts on the upper face-sheet.

5.1.1. LM25 sandwich beams

The measured collapse responses of beams L1 and L2 with spans $L = 110$ and 190 mm, respectively, are shown in Fig. 11a. The load increases monotonically with deflection until the struts inclined to the roller axis on the lower face-sheet fail in tension. This collapse mode was confirmed by measurements from the three clip gauges and two strain gauges mounted on the specimens. The readings from these gauges are plotted against the relative displacement of the central and two outer support rollers in Fig. 11b for the specimen L1 ($L = 110$ mm). The largest strain levels are experienced in the face struts inclined to the roller

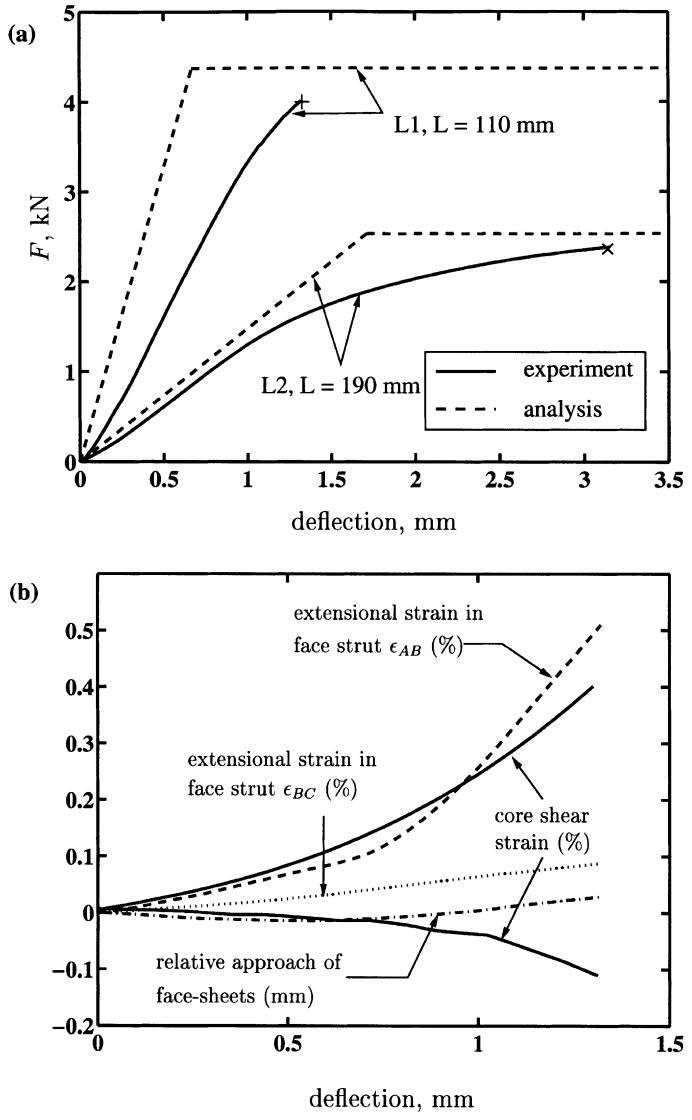

Fig. 11. (a) Measured and predicted load versus displacement response of the LM25 double layer grid in 3-point bending, with a span $L = 110$ and 190 mm. The prediction gives the elastic response and the limit load for the perfectly plastic solid. (b) Measured clip gauge and strain gauge readings for the LM25 double layer grid of span $L = 110$ mm. The specimen geometry and location of gauges are shown in Fig. 10.

axis, while relatively low levels of strain are experienced by the core struts: we conclude that collapse is by face yield, with core shear and indentation modes inoperative.

The predictions for beam stiffness, Eq. (13a)–(13c), and limit load, Eq. (14), are included in Fig. 11a. These predictions employ Eqs. (1a) and (4b) to estimate E_{11}^{f} and σ_{11}^{fY}, respectively, while G_{13}^{c} is calculated from Eq. (2b). The measured peak loads are in good agreement with the predictions for both span, $L = 110$ mm and 190 mm. However, the predicted stiffness for the $L = 110$ mm case is higher than the measured value. This can be traced to the fact that the predicted shear stiffness G_{13}^{c} exceeds the measured value due to the local shearing and bending deflections of the pins of the tetrahedral core, recall Fig. 8a.

5.1.2. MB1 sandwich beams

The collapse responses of beams M1 and M2 with spans $L = 110$ mm and $L = 190$ mm, respectively, are shown in Fig. 12. Wrinkling occurs in both cases, due to plastic buckling of the upper face-sheet struts. The struts buckle without rotation of the nodes and thus the buckling stress σ_c is given by Eq. (9) with $k = 2$; the wrinkling stress σ_{11}^{fW} for the triangulated face-sheets follows from Eq. (10b). The face wrinkling limit load, F_{FW}, estimated from Eq. (15) is included in Fig. 12 for each beam. These limit load predictions are lower than the measured peak loads due to the large rotations of the MB1 sandwich beams prior to buckling; this effect has been neglected in the limit load analysis since it assumes infinitesimal straining. As for the LM25 beams, the predicted beam stiffness is in satisfactory agreement with the measured value for the $L = 190$ mm beam but overestimates the stiffness of the $L = 110$ mm beam. Again, the source of the discrepancy is the shearing and bending of the core pins in shear.

5.2. Sandwich beams with solid face-sheets

The collapse responses of the LM25 and MB1 sandwich beams with solid face-sheets (specimens L3, L4, M3 and M4 of Table 1) are detailed in this section. In all cases, collapse was by core shear. It is worth

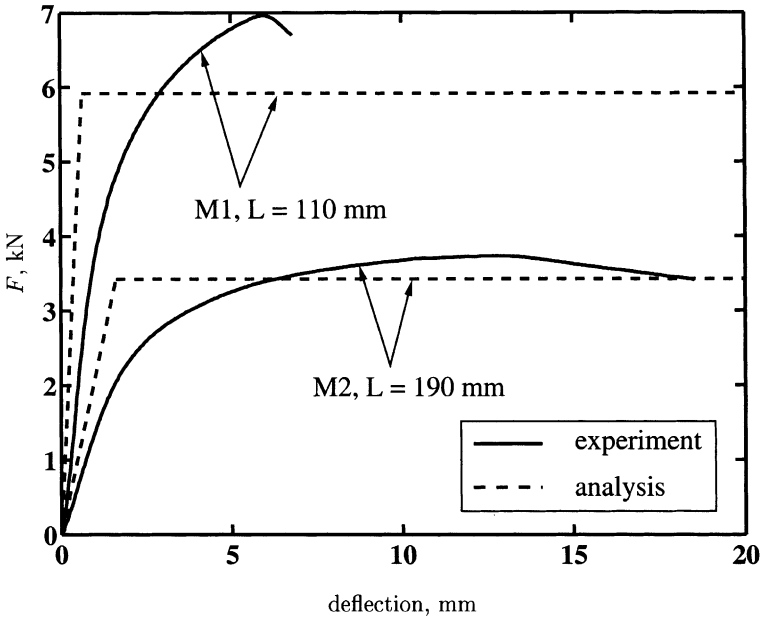

Fig. 12. Measured and predicted load versus displacement response of the MB1 double layer grid in 3-point bending, with a span $L = 110$ and 190 mm. The prediction gives the elastic response and the limit load for the strain hardening solid.

mentioning here that beams L4 and M4, with span $L = 190$ mm, have a variability of face-sheet thickness of $\pm 30\%$ over the length of the beams, due to casting misruns. Consequently, the plastic dissipation in the hinges formed in the face-sheets cannot be calculated accurately, and the agreement between predicted and measured strengths is poor.

In all cases the beam stiffness predicted by Eqs. (13a)–(13c) exceeds the measured value. This is a consequence of the fact that the centre-lines of the struts do not meet on the mid-plane of the face-sheets; additional shear deformation and bending of the pins occur at the attachment points between the tetrahedral core and the face-sheets.

5.3. LM25 sandwich beams

The load versus deflection curves of specimens L3 and L4 are plotted in Fig. 13. Measurements of the bending strains by the strain gauge rosette on the lower face-sheet, and measurements of the shear strain in the core by clip-gauges, confirmed that the beams deform in Mode B core shear. The peak load corresponds to the onset of shearing of the pins of the tetrahedral truss core.

The predicted limit load for pin shear is given by Eq. (16b), with σ_{13}^{cY} given by Eq. (12): the prediction agrees well with the measured peak load for beam L3 with a span length $L = 110$ mm. However, the agreement between the measured and predicted responses of specimen L4 with $L = 190$ mm (Fig. 13a) is poor for the reasons detailed above. It is worth mentioning here that the specimens L3 and L4 had an overhang length $H = 45$ mm which exceeds the transition value $H = 18$ mm (Eq. (17)), and so core shear occurs in Mode B.

5.4. MB1 sandwich beams

The MB1 beams also collapsed by Mode B core shear. The load versus deflection responses of specimens M3 and M4 are plotted in Fig. 13b; the peak load corresponds to shear failure of the joints between the tetrahedral core and the face-sheets. Note that the predicted limit load for $L = 110$ mm is lower than the measured peak value. This is because we underestimated the strength of the hinges formed in the face-sheets by employing the MB1 yield strength $\sigma_{11}^{fY} = 100$ MPa in Eq. (16b): strain-hardening of the MB1 increases the contribution to the strength from the face-sheets.

6. Minimum weight design

Truss core sandwich beams can be optimised to minimise weight against design constraints such as collapse load, beam stiffness or some other structural index. In this section we shall minimise the weight of sandwich beams with a tetrahedral truss core and solid face-sheets [3] made from the same material and subjected to a given collapse load F in 3-point bending. We begin by stating the geometry, collapse load and beam weight in non-dimensional terms. The non-dimensional face-sheet thickness $\bar{t}$, core thickness $\bar{c}$ and strut aspect ratio $\bar{a}$ are defined by

$$\bar{t} \equiv t/L, \quad \bar{c} \equiv c/L \quad \text{and} \quad \bar{a} \equiv a/l, \tag{19}$$

respectively. The non-dimensional weight of the sandwich beam $\bar{M}$ is related to the weight M of the beam by

[3] Wicks and Hutchinson (2001) have recently shown that truss core beams with solid face-sheets are always more weight-efficient in carrying bending and shear loads than truss-core beams with triangulated faces.

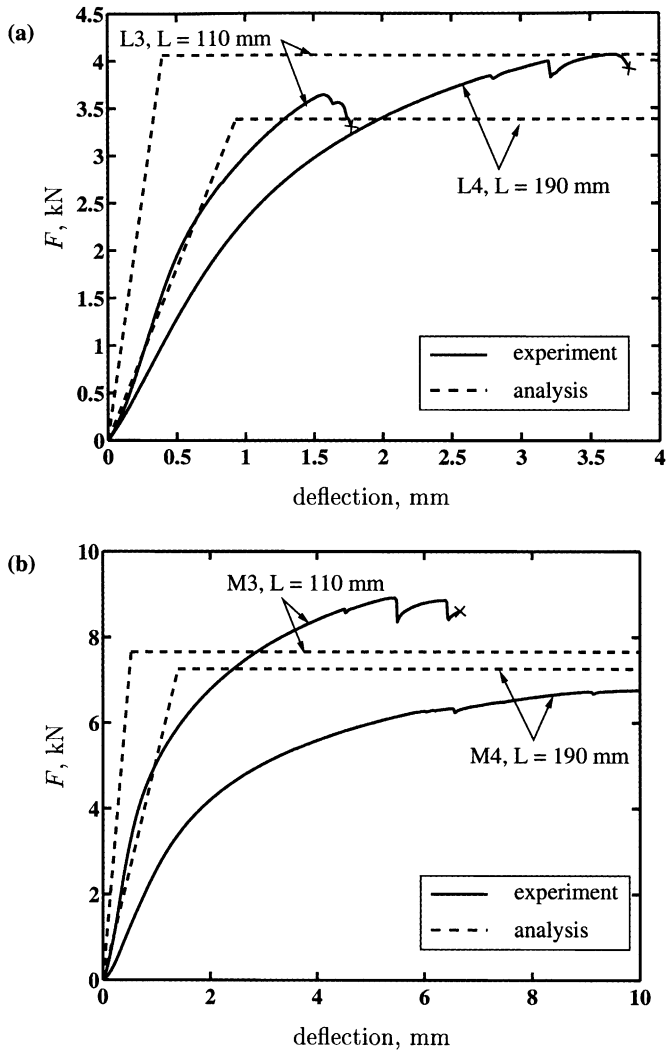

Fig. 13. Measured and predicted load versus displacement responses of (a) LM25 and (b) MB1 beams with solid face-sheets.

$$\bar{M} = \frac{M}{\rho b L^2} = 2\bar{t} + 3\sqrt{2}\pi\bar{c}\bar{a}^2, \tag{20}$$

where ρ is the density of the struts and face-sheets. The non-dimensional structural load index $\bar{F}$ is related to the collapse load F by

$$\bar{F} = \frac{F}{bL\sigma_Y}, \tag{21}$$

where σ_Y is the yield strength of the struts and face-sheets. Expressions for $\bar{F}$ follow from Eqs. (14), (16b) and (18) as

$$\bar{F}_{FY} = 4\bar{t}(\bar{c} + \bar{t}), \tag{22}$$

for face yield,

$$\bar{F}_{\mathrm{CS}}^{\mathrm{B}} = 4\bar{t}^2 + 2\pi\bar{c}\bar{a}^2, \tag{23}$$

for core shear in Mode B, and

$$\bar{F}_{\mathrm{I}} = 2^{11/4}\sqrt{\pi\bar{t}\bar{a}}, \tag{24}$$

for indentation. In the above expressions we have employed $\sigma_{33}^{\mathrm{cY}}$ and $\sigma_{13}^{\mathrm{cY}}$ as given by Eq. (5a): plastic yielding of the struts is the assumed collapse mode for core shear and indentation. It remains to specify the face-wrinkling collapse load $\bar{F}_{\mathrm{FW}}$ for truss core sandwich beams with solid face-sheets. Wicks and Hutchinson (2001) analysed the elastic buckling of face-sheets by assuming that the buckle wavelength is set by the inter-nodal distance between attachments to the core; further, they assumed a negligible restraint of the truss core to the buckling mode of the face-sheets. Upon making use of their analysis, the non-dimensional collapse load $\bar{F}_{\mathrm{FW}}$ is given by

$$\bar{F}_{\mathrm{FW}} = \frac{49\pi^2}{54(1-\nu^2)\epsilon_{\mathrm{Y}}}\frac{\bar{t}^3}{\bar{c}^2}(\bar{c}+\bar{t}), \tag{25}$$

where ν and ϵ_{Y} are the elastic Poisson's ratio and yield strain of the face-sheets.

For a prescribed strut aspect ratio $\bar{a}$, the optimal design is obtained by selecting the beam geometry $(\bar{t},\bar{c})$ which minimises the weight $\bar{M}$ for a given structural load index $\bar{F}$. To help with this optimisation, it is instructive to construct a collapse mechanism map for the truss core sandwich beams with solid face-sheets along the lines of those plotted by Chen et al. (2001) and Bart-Smith et al. (2001) for sandwich beams with metallic foam cores. In constructing such a map it is assumed that the operative collapse mechanism is the one associated with the lowest collapse load. An example of such a map with $\bar{a} = 0.07$ and solid material parameters $\nu = 1/3$ and $\epsilon_{\mathrm{Y}} = 0.007$ is shown in Fig. 14 with the non-dimensional axes $\bar{c} = c/L$ and $t/c = \bar{t}/\bar{c}$. It is worth mentioning here that the beam theory formulae of Section 4.2 used in constructing this failure mechanism map are not expected to be valid for $\bar{t}$ and $\bar{c} > 0.5$ and thus the axes have been truncated at these values. The regimes of dominance for each collapse mechanism are marked: face-wrinkling dominates for the values of the parameters selected. For the purpose of selecting minimum weight geometries contours of $\bar{M}$ and $\bar{F}$ have been added to the collapse mechanism map. Both $\bar{F}$ and $\bar{M}$ increase along the leading diagonal of the map, with increasing $\bar{c}$ and $\bar{t}/\bar{c}$. We note that the minimum weight design for any value of structural load index $\bar{F}$ is attained along the boundaries of the collapse regimes. The arrows shown in Fig. 14 designate the path of minimum weight design with diminishing $\bar{F}$.

Explicit expressions for the minimum weight designs along the boundaries of the collapse mechanism map can be obtained in a straightforward manner; however, such expressions are lengthy and are omitted here for the sake of brevity. The minimum weight $\bar{M}_{\min}$ is plotted as a function of $\bar{F}$ in Fig. 15a for the above case ($\bar{a} = 0.07$, $\nu = 1/3$, $\epsilon_{\mathrm{Y}} = 0.007$), and the associated optimal geometrical parameters are included in the figure.

It is instructive to explore the effect of strut aspect ratio $\bar{a}$ upon the minimum weight $\bar{M}_{\min}$, for values of $\bar{a}$ achievable by current manufacturing technologies. The results are shown in Fig. 15b for $\bar{a} = 0.07$ and $\bar{a} = 0.09$: note that the choice $\bar{a} = 0.07$ gives lower $\bar{M}_{\min}$ values at low values of $\bar{F}$, whereas the choice $\bar{a} = 0.09$ gives lower weights at higher levels of $\bar{F}$.

The point has already been made at the beginning of this article that sandwich beams with a stretching-governed truss core are more weight efficient at carrying structural loads than sandwich beams with a metallic foam core. We proceed by comparing explicitly the minimum weights of these two competing concepts. For simplicity, consider a sandwich beam with a foam core and face-sheets made from the same solid material of yield strength σ_{Y}. Further, assume that the compressive strength $\sigma_{\mathrm{foam}}^{\mathrm{Y}}$ and the shear $\tau_{\mathrm{foam}}^{\mathrm{Y}}$ strength of the foam core are related to the relative density $\bar{\rho}$ of the foam via (Ashby et al., 2000),

$$\sigma_{\mathrm{foam}}^{\mathrm{Y}} = 0.25\bar{\rho}^{1.5} \tag{26}$$

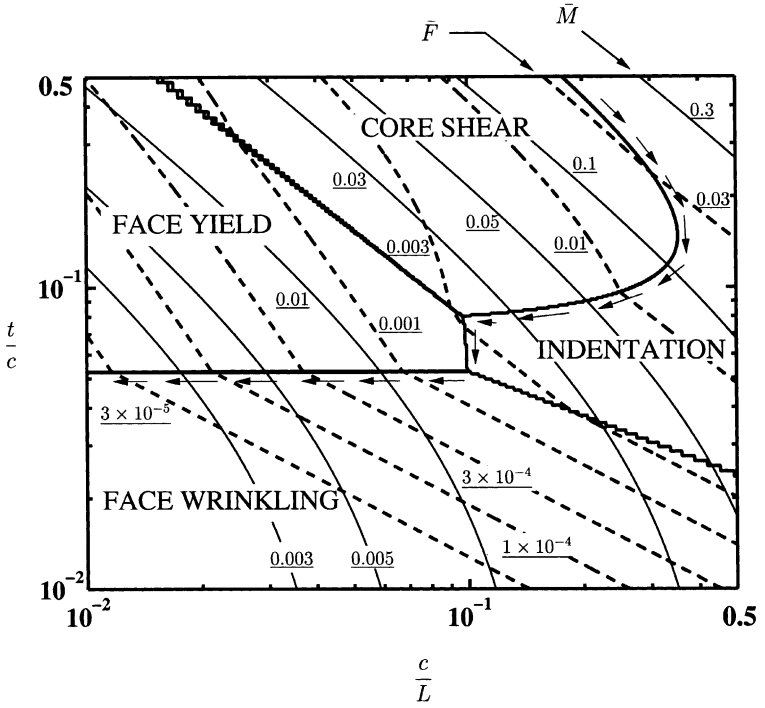

Fig. 14. Collapse mechanism map for truss core sandwich beams with solid face-sheets loaded in 3-point bend for $\bar{a} \equiv a/l = 0.07$, $\epsilon_Y = 7 \times 10^{-3}$ and $v = 1/3$. Contours of dimensionless weight $\bar{M}$ and the structural load index $\bar{F}$ have been added. The arrows trace the path of minimum weight designs with diminishing $\bar{F}$.

and

$$\tau^{Y}_{foam} = \tfrac{2}{3}\sigma^{Y}_{foam}, \tag{27}$$

respectively. With these relations in hand for the foam strength, we calculate the minimum weight $\bar{M}_{min}$ of metallic foam core sandwich beams loaded in 3-point bend, in the manner outlined by Chen et al. (2001). Predictions for $\bar{\rho} \approx 0.06$ and 0.11 are included in Fig. 15b: the choice $\bar{\rho} \approx 0.06$ and 0.11 corresponds to the truss cores with $\bar{a} = 0.07$ and 0.09, respectively. Moreover, $\bar{\rho} = 0.11$ is typical for commercially available metallic foams. We note that the truss core sandwich beams are highly weight efficient compared with foam core sandwich beams particularly at the higher values of $\bar{F}$.

The optimisation results presented here are for fixed values of strut aspect ratios $\bar{a}$ as dictated by manufacturing constraints for investment casting. On the other hand, Wicks and Hutchinson (2001) allowed the strut aspect ratio $\bar{a}$ to vary and found global minimum weight designs using a numerical search algorithm. They report that the fully optimised designs lie on the boundaries between the collapse modes of face yield, elastic face wrinkling and elastic buckling of the core struts. Their global minimum is compared with the predictions for $\bar{a} = 0.07$ and 0.09 in Fig. 16. The optimal values of strut aspect ratio $\bar{a}$ are very low and increase from about 0.02 to 0.04 with increasing $\bar{F}$ over the selected range. It is concluded that the minimum weight design for $\bar{a} = 0.07$ has a mass which is about 30% greater than the global minimum of Wicks and Hutchinson (2001). It is anticipated that future advances in manufacturing technologies will yield substantial weight savings through reduced values of $\bar{a}$.

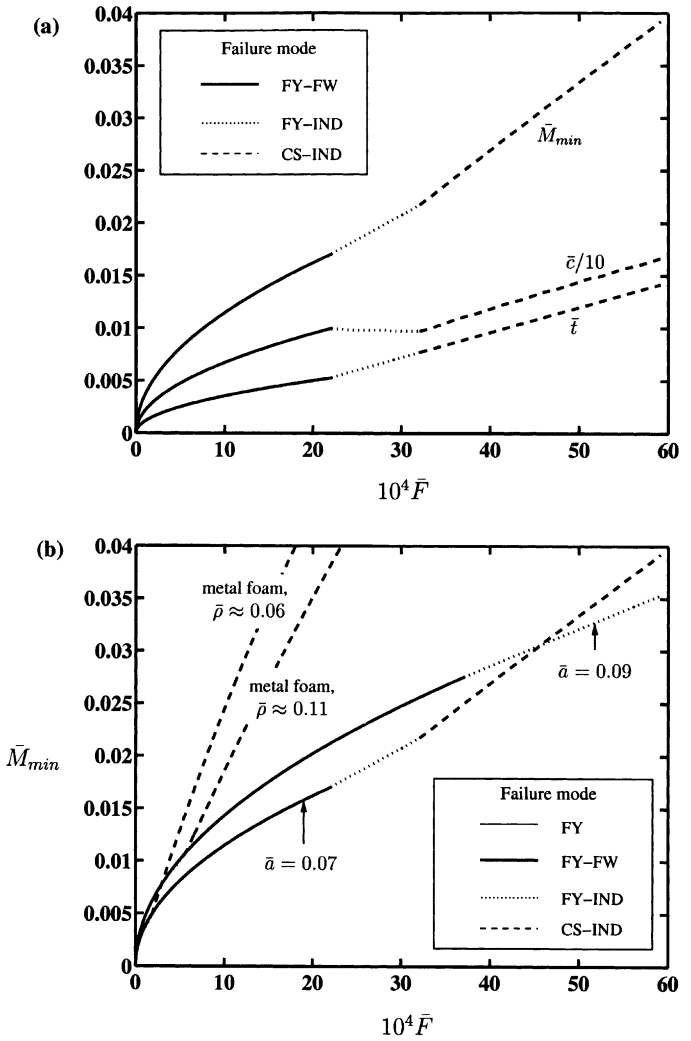

Fig. 15. Minimum weight designs for truss core sandwich beams with solid faces, $\epsilon_Y = 7 \times 10^{-3}$ and $\nu = 1/3$. Depending upon the assumed value of $\bar{F}$, collapse is by combined face yield and wrinkling (FY–FW), by combined face yield and indentation (FY–IND) or by combined core shear and indentation (CS–IND). (a) Details of design for strut aspect ratio $a/l = 0.07$. (b) Comparison of minimum weight design for selected strut aspect ratios $\bar{a}$ with that for a metallic foam core.

7. Concluding remarks

Truss-core sandwich beams with triangulated and solid faces have been investment cast in LM25 aluminium–silicon and MB1 silicon–brass alloys. The measured effective properties of the triangulated face-sheets and tetrahedral core agree well with the analytic predictions and their deformation is stretching-governed in most cases. However, shear failure of the tetrahedral core is by plastic shearing of the pins attaching the tetrahedral core to the face-sheets. The design of adequately stiff and strong joints that minimises the mass of the nodes is an important consideration in future refinements of these truss materials.

The analytic strength formulae given by limit load analyses are in good agreement with the measured collapse strengths of the truss core sandwich beams loaded in 3-point bend: the collapse modes of

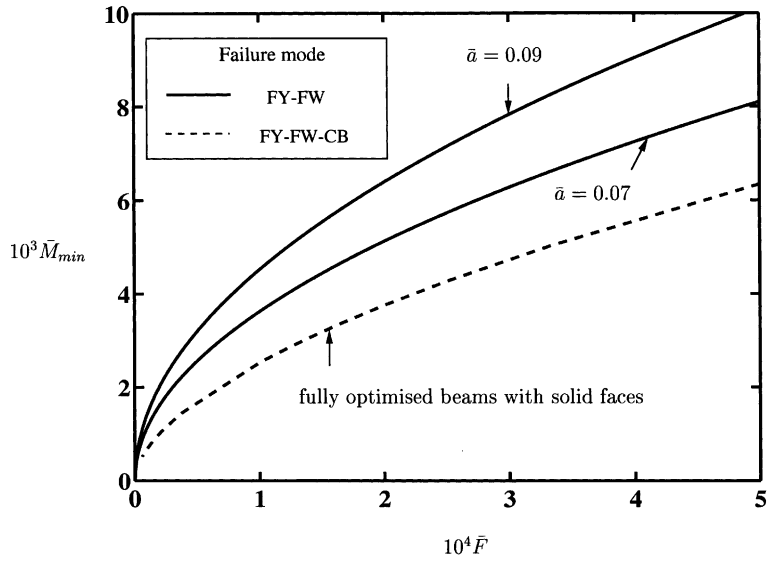

Fig. 16. Comparison of minimum weight designs for fully optimised truss core sandwich beams with solid faces (Wicks and Hutchinson, 2001) and designs with a/l fixed at 0.07 and 0.09, $\epsilon_Y = 7 \times 10^{-3}$ and $\nu = 1/3$. The fully optimised beams collapse by combined face yield, face wrinkling and elastic buckling of the core struts (FY–FW–CB) over the shown range of $\bar{F}$.

face-yield, face-wrinkling and core shear were each observed. The use of effective properties for the tetrahedral core and triangulated face-sheets is an acceptable simplification in predicting the beam response. The strength formulae for the sandwich beams are used in minimum weight design, and reveal that optimal sandwich beam designs lie at the boundaries of competing collapse modes. Moreover, the optimisation reveals that practical designs of truss core sandwich beams compare very favourably with the competing concept of metallic foam core sandwich beams from a weight standpoint.

Acknowledgements

The authors are grateful to DARPA/ONR for their financial support through MURI grant number N00014-1-96-1028 on the Ultralight Metal Structures project at Harvard University. The authors would like to thank Profs. M.F. Ashby, A.G. Evans and J.W. Hutchinson for helpful discussions, and S. Marshall and A. Heaver for help with the experiments.

Appendix A. Comparison of the stiffness and strength of tetrahedral and pyramidal truss cores

The pyramidal truss core competes with the tetrahedral truss-core for sandwich beam construction. Wallach and Gibson (2001) recently reported a finite element analysis of the stiffness and strength of a pyramidal truss core. [4] In this appendix we give approximate analytical expressions for the stiffness and strength of tetrahedral and pyramidal truss cores, comprising elastic–plastic, circular cylindrical struts of length l and radius a. It is straightforward to extend these formulae to the case of struts of arbitrary cross-section. We shall focus on the most pertinent properties of the core for sandwich panel applications: the

[4] JAM Corp., 17 Jospin Road, Wilmington, MA 01887-102, USA. Fax: +1-617-978-0080.

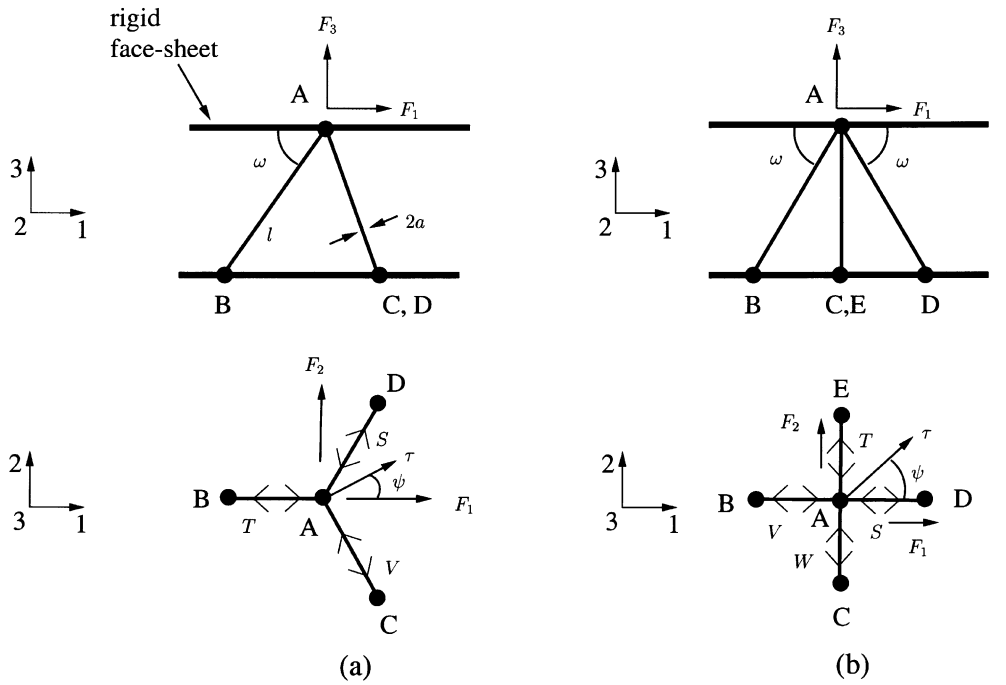

Fig. 17. Geometry of (a) tetrahedral core and (b) pyramidal core. (S, T, V) are the bar tensions of the tetrahedral truss and (S, T, V, W) are the bar tensions of the pyramidal truss due to a nodal force **F** applied to node A of each assembly.

out-of-plane axial stiffness E_{33} and strength σ_{33}, and the transverse shear stiffness G_{13} and G_{23}, and strengths σ_{13} and σ_{23}. The struts are ascribed a sufficiently low aspect ratio a/l for their bending stiffness and strength to be negligible compared to their stretching stiffness and strength. Thus, the core is treated as a frictionless pin-jointed truss.

Sketches of the tetrahedral and pyramidal truss cores with their associated Cartesian co-ordinate system are shown in Fig. 17. Here we consider truss cores sandwiched between rigid face-sheets, and consider the full range of core aspect ratios, as parameterised by the angle ω between the core struts and the faces.

A.1. Tetrahedral core

Consider first the stiffness and strength of a tetrahedral core, as sketched in Fig. 17a. The relative density of the core (defined by the density of the core divided by the density of the solid from which it is made) is

$$\bar{\rho} = \frac{2\pi}{\sqrt{3}} \frac{1}{\cos^2 \omega \sin \omega} \left(\frac{a}{l}\right)^2, \tag{A.1}$$

for a core occupying 50% of available tetrahedral sites, as shown in Fig. 1a. If, instead all of the tetrahedral sites are occupied then the formula (A.1) for $\bar{\rho}$ should be doubled. However, the predictions given below for stiffness and strength, and expressed in terms of $\bar{\rho}$, hold for any area fraction of tetrahedral sites occupied by the core. The normal modulus E_{33} is deduced by applying a point load **F** with single component F_3 to the apex node A of a representative tetrahedron, as defined in Fig. 17a, and by calculating the resulting normal displacement of the two face-sheets. Consequently, we obtain

$$\frac{E_{33}}{E_S} = \bar{\rho}\sin^4\omega = \frac{2\pi}{\sqrt{3}}\frac{\sin^3\omega}{\cos^2\omega}\left(\frac{a}{l}\right)^2. \tag{A.2}$$

Triangular symmetry implies transverse isotropy of elastic properties, such that the transverse shear modulus of the core is independent of orientation within the 1–2 plane, giving $G_{13} = G_{23}$. The shear modulus G_{13} is deduced by applying the single force component F_1 to node A, and by determining the work-conjugate nodal displacement, to get

$$\frac{G_{13}}{E_S} = \frac{\bar{\rho}}{8}\sin^2 2\omega = \frac{\pi}{\sqrt{3}}\sin\omega\left(\frac{a}{l}\right)^2. \tag{A.3}$$

Now consider the strength of the tetrahedral truss. The normal strength σ_{33} is associated with the simultaneous yield of all three bars, and is given by

$$\frac{\sigma_{33}}{\sigma_Y} = \bar{\rho}\sin^2\omega = \frac{2\pi}{\sqrt{3}}\frac{\sin\omega}{\cos^2\omega}\left(\frac{a}{l}\right)^2, \tag{A.4}$$

for both tensile and compressive loading. The transverse shear strength is specified in terms of the magnitude of shear strength τ and its direction ψ with respect to the x_1-axis, as defined in Fig. 17a,

$$\sigma_{13} = \tau\cos\psi, \quad \sigma_{23} = \tau\sin\psi, \quad \sigma_{33} = 0. \tag{A.5}$$

Equilibrium dictates the relation between the force **F** on node A and the macroscopic shear stress τ, such that

$$F_1 = 2A\sigma_{13}, \quad F_2 = 2A\sigma_{13}, \quad F_3 = 0, \tag{A.6}$$

where

$$A = \frac{3\sqrt{3}}{4}l^2\cos^2\omega \tag{A.7}$$

is the area of the base triangle of each tetrahedron in the (x_1, x_2) plane. The factors of two in Eq. (A.6) arise because only 50% of the tetrahedral sites are assumed to be occupied, consistent with the definition (A.1) for $\bar{\rho}$.

Each pin-jointed tetrahedron is statically and kinematically determinate and so the tetrahedral core has the property that the initial yield surface and limit yield surface coincide for struts made from an elastic–ideally plastic solid. On assuming that the single bar tension T (see Fig. 17a) attains the yield value $T = \pi a^2\sigma_Y$, the magnitude τ of the in-plane shear strength depends upon the orientation of in-plane loading according to

$$\frac{\tau}{\sigma_Y} = \frac{\bar{\rho}}{4}\frac{\sin 2\omega}{\cos\psi} = \frac{\pi}{\sqrt{3}}\frac{1}{\cos\omega\cos\psi}\left(\frac{a}{l}\right)^2, \tag{A.8}$$

for $|\psi| \leqslant \pi/6$. If instead, it is assumed that the single bar tension S attains the compressive yield value $S = -\pi a^2\sigma_Y$, then the macroscopic shear strength is

$$\frac{\tau}{\sigma_Y} = \frac{\bar{\rho}}{2}\frac{\sin 2\omega}{\left(\cos\psi + \sqrt{3}\sin\psi\right)} = \frac{2\pi}{\sqrt{3}}\frac{1}{\left(\cos\psi + \sqrt{3}\sin\psi\right)\cos\omega}\left(\frac{a}{l}\right)^2, \tag{A.9}$$

for $\pi/6 \leqslant \psi \leqslant \pi/2$. The solution for τ is periodic in ψ, with a period of $2\pi/3$, and reflects the symmetry of the structure. Each plane of the yield surface corresponds to a single strut attaining tensile or compressive yield, as summarised in Fig. 18a. Thus, the in-plane shear strength fluctuates with ψ between the minimum value,

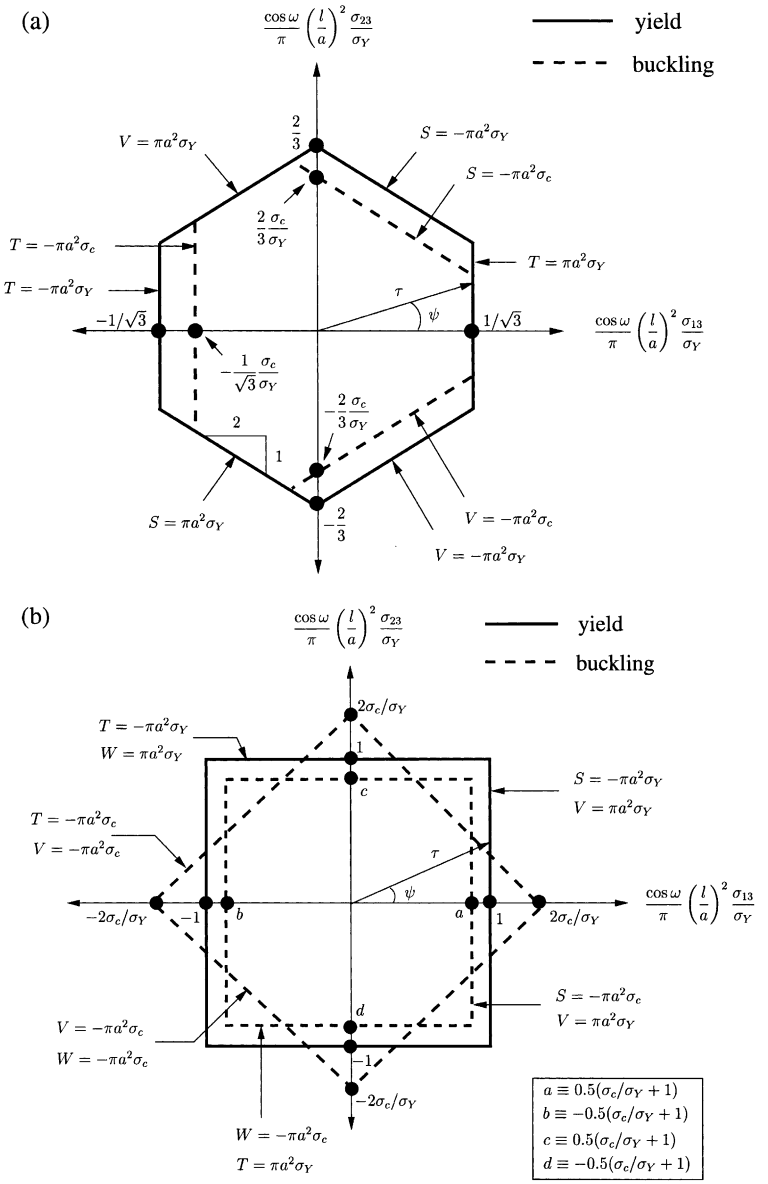

Fig. 18. Yield and buckling collapse surfaces in transverse shear for (a) tetrahedral and (b) pyramidal core. The collapse modes in (b) have only been partially labelled for the sake of clarity. The collapse modes of the unlabelled collapse planes follow from symmetry.

$$\frac{\tau_{\min}}{\sigma_Y}=\frac{\bar{\rho}}{4}\sin 2\omega=\frac{\pi}{\sqrt{3}}\frac{1}{\cos\omega}\left(\frac{a}{l}\right)^2, \tag{A.10}$$

at $\psi = n\pi/3$, and the maximum value

$$\frac{\tau_{\max}}{\sigma_Y}=\frac{\bar{\rho}}{2\sqrt{3}}\sin 2\omega=\frac{2\pi}{3}\frac{1}{\cos\omega}\left(\frac{a}{l}\right)^2, \tag{A.11}$$

at $\psi = \pi/6 + n\pi/3$, where the integer n ranges from 0 to 5.

The compressive strength σ_{33} and the transverse shear strength τ are degraded when the strut buckling stress σ_c, as given by Eq. (7), is less than the material yield strength σ_Y; then, the expression (A.4) still pertains, but with the factor σ_Y replaced by σ_c. Similarly, the segments of the shear yield surface $\tau(\psi)$ which are associated with compressive yield of one of the struts are similarly reduced in magnitude: the relations (A.8) and (A.9) hold, but with σ_Y replaced by σ_c, as shown diagrammatically in Fig. 18a.

A.2. Pyramidal core

A similar analysis can be conducted for the normal and shear stiffness and strength of a pyramidal truss core, as sketched in Fig. 17b. The relative density $\bar{\rho}$ of this core is

$$\bar{\rho} = \frac{2\pi}{\cos^2\omega \sin\omega}\left(\frac{a}{l}\right)^2, \tag{A.12}$$

and the normal modulus E_{33} is given by

$$\frac{E_{33}}{E_S} = \bar{\rho}\sin^4\omega = 2\pi\frac{\sin^3\omega}{\cos^2\omega}\left(\frac{a}{l}\right)^2. \tag{A.13}$$

As for the tetrahedral core, the truss core has a sufficient degree of symmetry for the transverse shear modulus to be isotropic, and

$$\frac{G_{13}}{E_S} = \frac{G_{23}}{E_S} = \frac{\bar{\rho}}{8}\sin^2 2\omega = \pi\sin\omega\left(\frac{a}{l}\right)^2. \tag{A.14}$$

The normal collapse strength σ_{33} is attained when all four bars yield simultaneously in tension or in compression, and equilibrium provides the relation

$$\frac{\sigma_{33}}{\sigma_Y} = \bar{\rho}\sin^2\omega = 2\pi\frac{\sin\omega}{\cos^2\omega}\left(\frac{a}{l}\right)^2. \tag{A.15}$$

The transverse shear strength τ is dependent upon the loading direction ψ as defined in Fig. 17b. The yield surface consists of a locus of collapse planes, with each plane corresponding to one strut undergoing tensile yield, the opposing strut compressive yield, and the remaining two struts remaining rigid. For example, assume that the bar AB of Fig. 17b yields in tension under the force $V = \pi a^2\sigma_Y$, the bar AD yields in compression under the force $S = -\pi a^2\sigma_Y$ while the remaining bars AC and AE remain rigid but not necessarily stress free. Then, the shear strength $\tau(\psi)$ is given by

$$\frac{\tau(\psi)}{\sigma_Y} = \frac{\bar{\rho}}{4}\frac{\sin 2\omega}{\cos\psi} = \frac{\pi}{\cos\omega\cos\psi}\left(\frac{a}{l}\right)^2, \tag{A.16}$$

for $|\psi| \leqslant \pi/4$. We conclude that $\tau(\psi)$ is periodic in ψ, with a period of $\pi/2$, and constitutes a square in stress space, see Fig. 18b; with increasing ψ, the magnitude τ fluctuates between the minimum value $(1/4)\bar{\rho}\sigma_Y \sin 2\omega$ and the maximum value $(\sqrt{2}/4)\bar{\rho}\sigma_Y \sin 2\omega$.

When the buckling stress σ_c of the struts is less than the material yield strength σ_Y, the compressive and transverse shear strengths are degraded. The compressive strength σ_{33} of the pyramidal core is still given by Eq. (A.15) but with σ_Y replaced by σ_c. On the other hand, transverse shear can trigger two distinct collapse mechanisms involving buckling of the bars.

(i) Collapse modes which involve the simultaneous tensile yield and buckling of opposing bars. For example, bar AB yields in tension at a stress σ_Y while bar AD buckles at a stress σ_c, with bars AC and AE remaining rigid but not necessarily stress-free. Then formula (A.16) still applies but with σ_Y replaced by $(\sigma_Y + \sigma_c)/2$: the collapse surface in this case is an inner square, as sketched in Fig. 18b.

(ii) Adjacent bars buckling at a stress σ_c with the other two bars remaining rigid. For example, bar AD and bar AE buckle in compression under the force $S = -\pi a^2 \sigma_c$ and $T = -\pi a^2 \sigma_c$, respectively, while bars AB and AC remain rigid. The shear strength $\tau(\psi)$ is then given by

$$\frac{\tau(\psi)}{\sigma_c} = \frac{\bar{\rho}}{2} \frac{\sin 2\omega}{(\cos\psi + \sin\psi)} = \frac{2\pi}{\cos\omega} \frac{1}{(\cos\psi + \sin\psi)} \left(\frac{a}{l}\right)^2. \tag{A.17}$$

In this case the collapse surface is the rotated square shown in Fig. 18b.

The dominant failure mode depends upon the value of σ_c/σ_Y, as follows. Plastic yielding of the bars, Eq. (A.16), occurs for $\sigma_c/\sigma_Y > 1$. When $1 > \sigma_c/\sigma_Y > 0.5$ the shear strength is the inner envelope of the collapse surfaces (i) and (ii) (this is the case sketched in Fig. 18b). For $\sigma_c/\sigma_Y < 0.5$, the macroscopic strength $\tau(\psi)$ is governed by mechanism (ii) and Eq. (A.17) applies for all ψ.

A.3. Comparison of performance of tetrahedral and pyramidal truss cores

It is striking that the normal stiffness E_{33} and strength σ_{33}, and the transverse shear stiffness G_{13} are the same for both geometries of core, at a given relative density $\bar{\rho}$ and strut inclination angle ω. Further, the minimum value of transverse shear strength $\tau(\psi)$ is identical for the two types of core. However, the degree of anisotropy in shear strength is greater for the pyramidal core: the maximum value τ_{max} is 41% above the minimum value for the pyramidal core, whereas τ_{max} exceeds τ_{min} by 15% for the tetrahedral core.

The shear stiffness and strength for both the tetrahedral and pyramidal cores are maximised by choosing a strut inclination $\omega = \pi/4 = 45°$ by Eqs. (A.3), (A.8), (A.14) and (A.16): the choice $\omega = \arcsin\sqrt{2/3} \approx 55°$ adopted in the body of this paper gives a core shear stiffness and strength which is 6% below the optimal value. In contrast, the normal stiffness and strength at fixed $\bar{\rho}$ are maximised by selecting ω as close to $\pi/2$ as practically viable.

References

Allen, H.G., 1969. Analysis and design of structural sandwich panels. Pergamon Press, Oxford.

Ashby, M.F., Evans, A.G., Fleck, N.A., Gibson, L.J., Hutchinson, J.W., Wadley, H.N.G., 2000. Metal Foams: A Design Guide. Butterworth Heinemann, London.

ASTM Standard C273-94, 1994. Standard Test Method for Shear Properties of Sandwich Core Materials. American Society for Testing and Materials.

Bart-Smith, H., Hutchinson, J.W., Evans, A.G., 2001. The measurement and analysis of the structural performance of cellular metal sandwich construction. International Journal of Mechanical Sciences, in press.

Chen, C., Lu, T.J., Fleck, N.A., 1999. Effect of imperfections on the yielding of two-dimensional foams. Journal of Mechanics and Physics of Solids 47 (11), 2235.

Chen, C., Harte, A.-M., Fleck, N.A., 2001. The plastic collapse of sandwich beams with a metallic foam core. International Journal of Mechanical Sciences 43 (6), 1483.

Deshpande, V.S., Fleck, N.A., 2000. Isotropic constitutive models for metallic foams. Journal of Mechanics and Physics of Solids 48 (6–7), 1253.

Deshpande, V.S., Ashby, M.F., Fleck, N.A., 2001a. Foam topology: bending versus stretching dominated architectures. Acta Materialia 49, 1035.

Deshpande, V.S., Fleck, N.A., Ashby, M.F., 2001b. Effective properties of the octet-truss lattice material. Journal of Mechanics and Physics of Solids, in press.

Fuller, R.B., 1961. Octet truss. US Patent. Serial no. 563,931.

Hunt, H.E.M., 1993. The mechanical strength of ceramic honeycomb monoliths as determined by simple experiments. Transactions of the Institution of Chemical Engineers 71 A, p. 257–66.

Wallach, J.C., Gibson, L.J., 2001. Mechanical behaviour of a three-dimensional truss material. International Journal of Solids and Structures, in press.

Wicks, N., Hutchinson, J.W., 2001. Optimal truss plates. International Journal of Solids and Structures, in press.